Neuron

Article

Two translocation mechanisms drive neural stem cell dissemination into the human fetal cortex

Graphical abstract

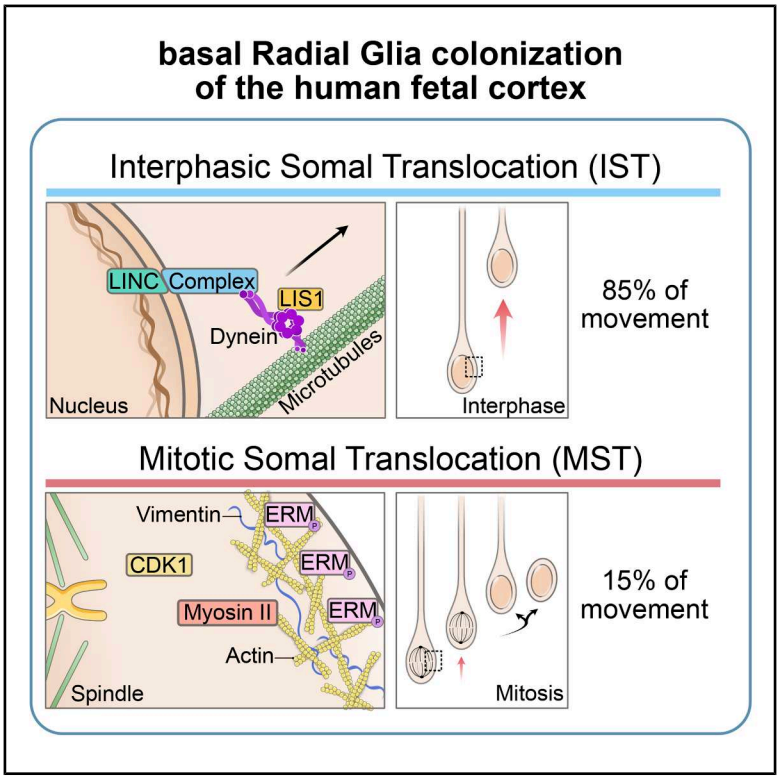

Highlights

- Interphasic translocation of the nucleus is dependent on dynein and microtubules
- Mitotic translocation of the spindle is dependent on the cell-rounding machinery
- IST is dominant over MST for bRG cell colonization in the human fetal cortex
- Both IST and MST also occur in glioblastoma cells via the same mechanisms

Authors

Ryszard Wimmer, Clarisse Brunet Avalos, Pauline Lestienne, ..., Julia Ladewig, Fabien Guimiot, Alexandre D. Baffet

Correspondence

alexandre.baffet@curie.fr

In brief

Wimmer et al. reveal how neural stem cells called basal radial glia move to build the expanded stem cell niche of the developing human cortex. They identify two distinct modes, one driven by microtubules in interphase and another by actomyosin in mitosis. These mechanisms are reused in migrating glioblastoma cells.

Wimmer et al., 2026, Neuron *114*, 1–18
June 17, 2026
https://doi.org/10.1016/j.neuron.2026.02.002

CellPress

Please cite this article in press as: Wimmer et al., Two translocation mechanisms drive neural stem cell dissemination into the human fetal cortex, Neuron (2026), https://doi.org/10.1016/j.neuron.2026.02.002

Neuron

CellPress
OPEN ACCESS

Article

Two translocation mechanisms drive neural stem cell dissemination into the human fetal cortex

Ryszard Wimmer,[1] Clarisse Brunet Avalos,[1,12] Pauline Lestienne,[1,12] Laure Coquand,[1] Amandine Di Cicco,[1] Christophe Chehade,[1] Annasara Artioli,[2,3,4] Matthieu Cortes,[5] Anna-Sophie Macé,[5] Xiuyu Wang,[6] Jean-Baptiste Manneville,[6] Bettina Bessière,[7] Ananya Roy,[8,9] Karin Forsberg-Nilsson,[8,9] Julia Ladewig,[2,3,4] Fabien Guimiot,[10] and Alexandre D. Baffet[1,11,13,*]

[1]Institut Curie, PSL University, Sorbonne Université, CNRS UMR144, Cell Biology and Cancer, 75005 Paris, France
[2]Department of Translational Brain Research, Central Institute of Mental Health, Medical Faculty Mannheim, Heidelberg University, Mannheim, Germany
[3]Hector Institute for Translational Brain Research (HITBR gGmbH), Mannheim, Germany
[4]German Cancer Research Center (DKFZ), Heidelberg, Germany
[5]UMR 144-Cell and Tissue Imaging Facility (PICT-IBiSA), CNRS, Institut Curie, Paris, France
[6]Laboratoire Matières et Systèmes Complexes, Université Paris Cité, CNRS UMR7057, 10 Rue Alice Domon et Léonie Duquet, Paris 75013, France
[7]UF Embryofœtopathologie, Hopital Necker-Enfants Malades, Paris, France
[8]Department of Immunology, Genetics and Pathology, Uppsala University, Uppsala 751 85, Sweden
[9]Science for Life Laboratory, Uppsala 752 37, Sweden
[10]UF de Fœtopathologie—Université de Paris et Inserm UMR1141, Hôpital Robert Debré, Paris, France
[11]Institut National de la Santé et de la Recherche Médicale (Inserm)
[12]These authors contributed equally
[13]Lead contact
*Correspondence: alexandre.baffet@curie.fr
https://doi.org/10.1016/j.neuron.2026.02.002

SUMMARY

The strong increase in the size of the human neocortex is supported by a neural stem cell population, the basal radial glial (bRG) cells. Using live imaging of human fetal tissue and cortical organoids, we identify two translocation mechanisms for bRG cell colonization of the human neocortex. On top of an actomyosin-dependent movement called mitotic somal translocation (MST), we identify a microtubule-dependent motion occurring during interphase that we call interphasic somal translocation (IST). We show that IST is driven by the dynein motor and its activator LIS1, which are recruited to the nuclear envelope by the LINC complex, while MST is controlled by the mitotic cell-rounding pathway. Eighty-five percent of bRG cell translocation is due to IST, resulting in a total movement of 0.67 mm per month of gestation. Our work identifies how bRG cells colonize the human fetal cortex and further shows that IST and MST also occur in bRG-related glioblastoma cells.

INTRODUCTION

The neocortex is a mammalian-specific brain structure that has expanded dramatically during recent primate evolution.[1,2] Neocortex expansion is largely supported by the neural stem cells—called the radial glial cells—that generate all neurons, astrocytes, and oligodendrocytes.[3–9] Two major types of radial glial cells coexist, with very different abundance and properties across mammals[10] (Figure 1A). Apical radial glial (aRG, also known as vRG) cells are common to all mammals and lie along the lateral ventricles, where they form a neuroepithelium.[11,12] At mid-neurogenesis, human aRG cells lose their connection to the pial surface, becoming truncated radial glia (tRG).[13] Basal radial glial (bRG, also known as outer radial glia [oRG]) cells, on the other hand, are rare and poorly proliferative in certain species, such as mice, but extremely abundant and proliferative in others, including primates or ferrets.[14–18] They furthermore appear to correlate with the degree of cortical folding.[10] bRG cells are particularly numerous in humans, where they are believed to underlie massive neocortical expansion. bRG cells are born from aRG cells and have delaminated, either through mitotic spindle rotation or interphasic loss of adherent junctions.[19,20] They form a second stem cell niche, located basally, called the outer subventricular zone (oSVZ).[21] How the human

Please cite this article in press as: Wimmer et al., Two translocation mechanisms drive neural stem cell dissemination into the human fetal cortex, Neuron (2026), https://doi.org/10.1016/j.neuron.2026.02.002

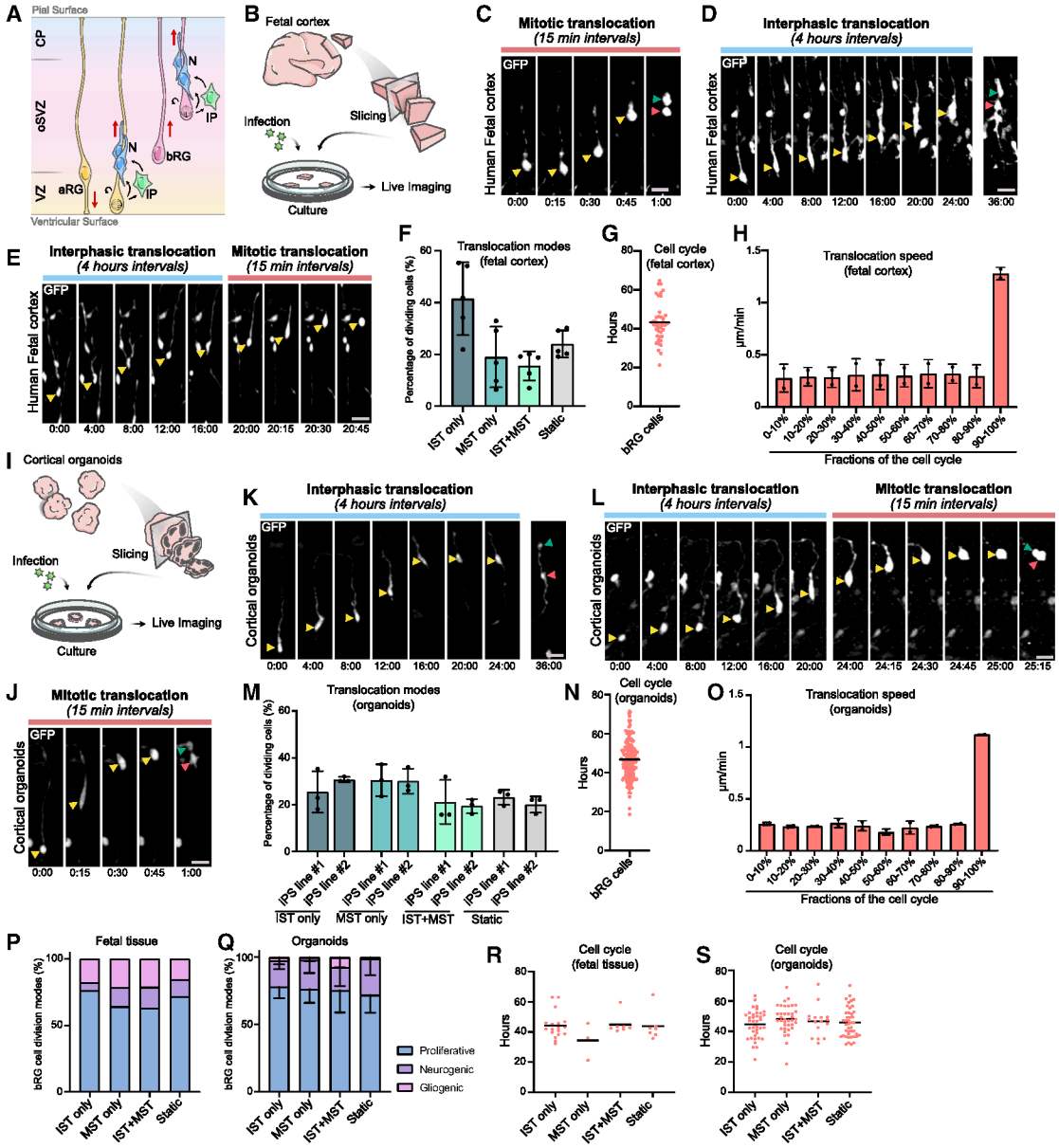

Figure 1. Slow interphasic and fast mitotic somal translocation

(A) Schematic representation of human neocortex development. VZ, ventricular zone; iSVZ and oSVZ, inner and outer subventricular zones; CP, cortical plate; aRG, apical radial glial; bRG, basal radial glia; IP, intermediate progenitor; and N, neuron.

(B) Procedure for human fetal cortex slicing, culture, infection, and live imaging.

(C) Live imaging of a GFP-expressing bRG cell performing mitotic somal translocation (MST) in human fetal tissue at pcw 14.

(D) Live imaging of a GFP-expressing bRG cell performing interphasic somal translocation (IST) in human fetal tissue at pcw 14.

(E) Live imaging of a GFP-expressing bRG cell performing IST followed by MST in human fetal tissue at pcw 15.

(F) Fraction of bRG cells undergoing IST only, MST only, or both in human fetal tissue at pcw 12–19 (n = 5 fetal samples, 476 bRG cells).

(G) Cell cycle duration of bRG cells in human fetal tissue at pcw 16. Cells were live imaged for 92 h, and cell cycle length was measured between two divisions (n = 2 fetal samples, 40 cells).

(H) Speed of bRG cell somal translocation throughout the cell cycle, between two consecutive divisions, in human fetal tissue pcw 16. The cell cycle was binned into 10 fractions (n = 2 fetal samples, 40 cells).

(I) Procedure for human cortical organoid slicing, culture, infection, and live imaging.

(J) Live imaging of a GFP-expressing bRG cell performing MST in a week 8 human cortical organoid.

(K) Live imaging of a GFP-expressing bRG cell performing IST in a week 8 human cortical organoid.

(L) Live imaging of a GFP-expressing bRG cell performing IST followed by MST in a week 9 human cortical organoid.

(legend continued on next page)

Please cite this article in press as: Wimmer et al., Two translocation mechanisms drive neural stem cell dissemination into the human fetal cortex, Neuron (2026), https://doi.org/10.1016/j.neuron.2026.02.002

oSVZ grows during the course of fetal development to support enhanced neuronal and glial cell production is only starting to be addressed.

Recent evidence has documented the high proliferative potential of human bRG cells.[22,23] oSVZ growth appears dominated by bRG cell symmetric self-amplifying divisions, coupled with a lower rate of self-consuming neurogenic divisions.[22] In cortical organoids, various treatments, such as optimized oxygenation or leukemia inhibitory factor (LIF) stimulation, increase the size of the oSVZ.[24–26] Likewise, overexpression of human-specific genes leads to the expansion of the bRG population and of the oSVZ.[27–34] Importantly, all these amplification events must be coupled to bRG cell dissemination into the growing oSVZ.

Most bRG cells are attached to the pial surface via an elongated process that can be several millimeters long. Once per cell cycle, prior to division, they undergo a so-called mitotic somal translocation (MST), whereby their soma rapidly advances within the process[15] (Figure 1A). This phenomenon was proposed to underlie the basal dissemination of bRG cells and the expansion of the oSVZ. bRG cells can adopt various morphologies, with a basal process (the most frequent shape), an apical process, two processes, or no process at all.[22,35,36] Consequently, MST can occur either basally or apically. MST is furthermore maintained in pre-oligodendrocyte progenitor cells (pre-OPCs) but over shorter distances.[37] MST is dependent on actomyosin contractility and the Rho-associated protein kinase (ROCK) but does not require microtubules.[19] mTOR signaling was further shown to modulate MST via regulation of the actin cytoskeleton and the morphology of bRG cells.[38] The exact molecular mechanism of MST, whether the microtubule cytoskeleton also controls other steps of bRG cell translocation, and the contribution of these movements to bRG cell dissemination into the human developing neocortex are, however, unknown.

Here, using live imaging of human fetal cortex tissue and human cortical organoids, we identify two independent modes of translocation for bRG cells. On top of actomyosin-dependent MST, bRG cells undergo a microtubule-dependent movement during interphase, which we call interphasic somal translocation (IST). IST accounts for 85% of total bRG cell movement, corresponding to a total of 0.67 mm per month of human fetal gestation. Finally, we demonstrate that IST and MST also occur in bRG-like glioblastoma cells and occur through the same molecular pathways. Overall, our work identifies how bRG cells colonize the human fetal neocortex and how alterations in these mechanisms can be linked to pathological conditions.

RESULTS

Fast MST and slow IST

To investigate bRG cell somal translocation, we used post-conceptional week (pcw) 12–20 human fetal cortical tissue and week 7–14 human cortical organoids, derived from two independent induced pluripotent stem (iPS) cell lines (STAR Methods; Figure S1A).[39,40] We observed typical elongated SOX2+ bRG cells and confirmed that these cells were positive for PAX6, HOPX, LIFR, PTPRZ1, and VIM (Figures S1B–S1E). They were discriminated from aRG cells based on their position above the VZ and because they were negative for the apical surface marker ZO-1, which marks all aRG cells (Figures S1D–S1F). Human fetal cortex was sliced and infected with green fluorescent protein (GFP)-coding retroviruses and live imaged for 2 to 4 days (Figure 1B). Live/fixed correlative imaging indicated that the majority of elongated OSVZ cells fixed before division were SOX2+[22] (Figures S1G and S1H). To unequivocally distinguish bRG cells from migrating neurons in live imaging, we only considered the cells that proceeded to mitosis. Moreover, interkinetic nuclear migration (INM)—which occurs in all aRG cells but not in bRG cells[41,42]—was used to distinguish these two cell types. Therefore, our four criteria for identifying bRG cells in live recordings were (1) elongation, (2) location in the OSVZ, (3) division, and (4) absence of INM.

Typical MST behavior could be identified in bRG cells right before cytokinesis (Figure 1C). Remarkably, we could also observe peculiar bRG cell somal translocation events occurring during interphase, albeit at a lower speed (Figure 1D). We named this process IST and observed that bRG cells could undergo IST only, MST only, or both (Figures 1E and 1F). We quantified the velocity of somal translocation throughout the entire cell cycle of bRG cells. Live imaging of fetal tissue for 4 days revealed an average cell cycle duration of 43 hours (h), around twice the duration of mouse aRG cells[43] (Figures 1G and S1I). Translocation velocity remained constant throughout interphase and greatly accelerated around mitosis, confirming the bi-phasic migration behavior (Figure 1H).

In cortical organoids, interphasic and mitotic translocation events were also observed, occurring at similar frequencies to those in fetal tissues (Figures 1I–1M and S1J). Four-day live imaging revealed a highly similar cell cycle duration for bRG cells (47 h), as well as comparable velocities to those in fetal tissue, both in interphase and mitosis (Figures 1N and 1O). Finally, we asked whether bRG cells undergoing IST only, MST only, both movements, or no movement could represent different subpopulations of bRG cells. Using live/fixed correlative imaging,[22] we

(M) Fraction of bRG cells undergoing IST only, MST only, or both in week 7–10 human cortical organoids (n = 3 organoid batches per iPS line, 314 bRG cells).
(N) Cell cycle duration of bRG cells in week 10–11 human cortical organoids. Cells were live imaged for 72 h, and cell cycle length was measured between two divisions (n = 2 organoid batches, 186 bRG cells).
(O) Speed of bRG cell somal translocation throughout the cell cycle, between two consecutive divisions, in week 10–11 human cortical organoids. The cell cycle was binned into 10 fractions (n = 2 organoid batches, 186 bRG cells).
(P) Division mode of bRG cells depending on translocation mode in human fetal tissue at pcw 16 (n = 1 fetal sample, 3 live-imaged slices, 110 cells).
(Q) Division mode of bRG cells depending on translocation mode in weeks 11–14 human cortical organoids (n = 5 organoid batches, 459 bRG cells).
(R) Cell cycle duration of bRG cells in human fetal tissue at pcw16 (n = 2 fetal samples, 40 cells).
(S) Cell cycle duration of bRG cells in week 10–11 human cortical organoids (n = 2 organoid batches, 186 bRG cells).
Yellow arrowheads indicate bRG cell soma, and green and red arrowheads indicate daughter cells. Data are presented as mean values ± SD. Scale bar, 20 μm. All live imaging montages are in h or min.

Please cite this article in press as: Wimmer et al., Two translocation mechanisms drive neural stem cell dissemination into the human fetal cortex, Neuron (2026), https://doi.org/10.1016/j.neuron.2026.02.002

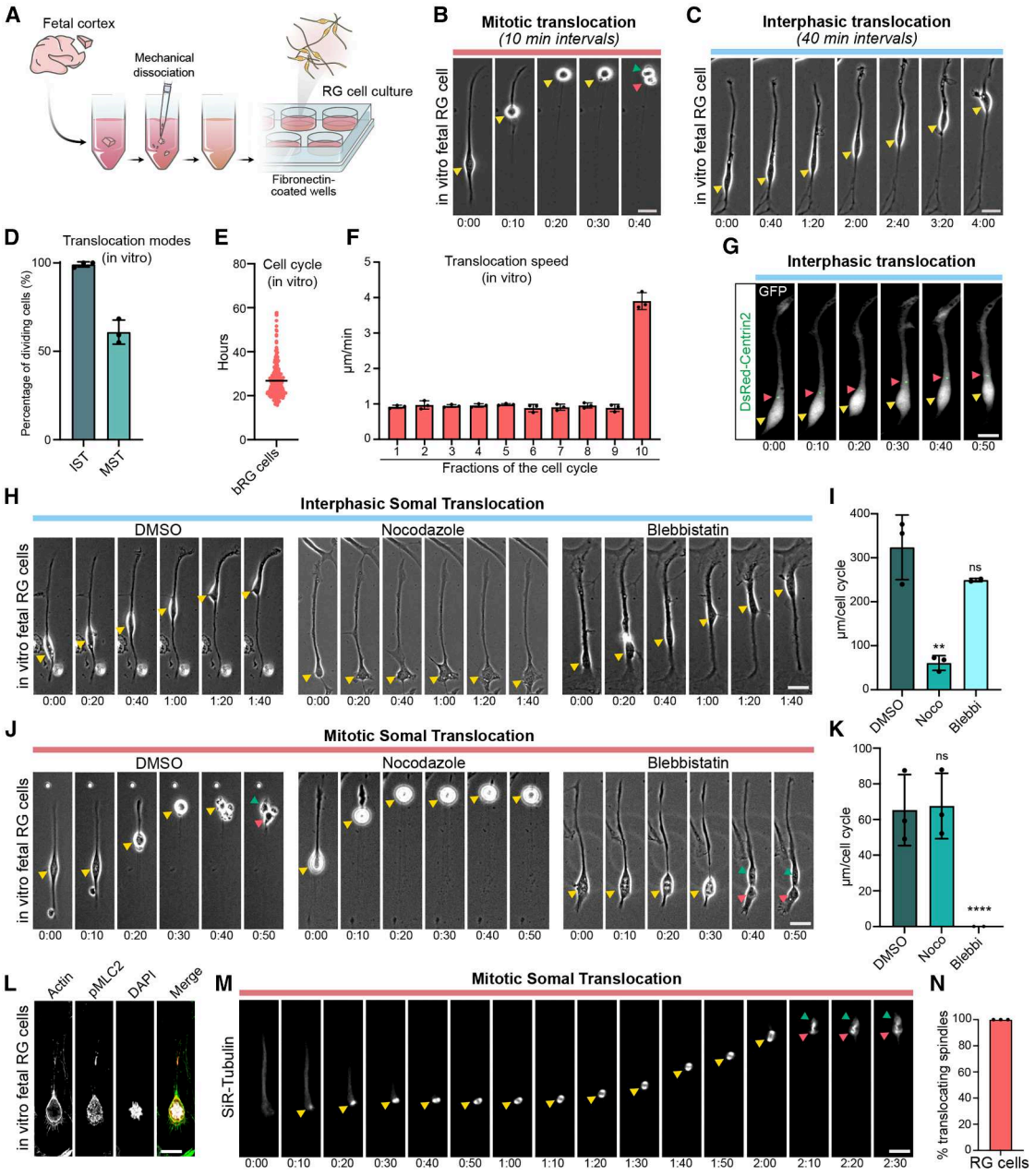

Figure 2. IST is microtubule dependent, and MST is actomyosin dependent

(A) Procedure for human fetal cortex dissociation, primary bRG cell 2-dimensional *in vitro* culture (*in vitro* bRG), and live imaging.

(B) Live imaging of an *in vitro* bRG cell performing MST.

(C) Live imaging of an *in vitro* bRG cell performing IST.

(D) Fraction of *in vitro* bRG cells undergoing IST and MST ($N = 3$ experiments, 240 bRG cells).

(E) Cell cycle duration of *in vitro* bRG cells. Cells were live imaged for 72 h, and cell cycle length was measured between two divisions ($n = 3$ experiments, 240 bRG cells).

(F) Speed of *in vitro* bRG cell somal translocation throughout the cell cycle, between two consecutive divisions. The cell cycle was binned into 10 fractions ($n = 3$ experiments, 240 bRG cells).

(G) Live imaging of an *in vitro* bRG cell performing IST and expressing GFP and DsRed-Centrin2.

(H) Live imaging of *in vitro* bRG cells during interphase, treated with DMSO, nocodazole (1 µM), or blebbistatin (10 µM).

(I) Quantification of IST amplitude following treatment with DMSO, nocodazole (1 µM), or blebbistatin (10 µM) in *in vitro* bRG cells ($n = 3$ experiments, 724 bRG cells).

(legend continued on next page)

Please cite this article in press as: Wimmer et al., Two translocation mechanisms drive neural stem cell dissemination into the human fetal cortex, Neuron (2026), https://doi.org/10.1016/j.neuron.2026.02.002

observed that the cellular output of dividing bRG cells was independent of their translocation mode in both fetal tissue and cortical organoids (Figures 1P, 1Q, and S1K). Likewise, the cell cycle duration of bRG cells did not differ depending on their translocation mode (Figures 1R and 1S). Therefore, bRG cells can undergo IST, MST, or both, but this does not correlate with different proliferative behaviors. Overall, human bRG cells translocate slowly throughout interphase and rapidly during mitosis, and this occurs both in human cortical organoids and fetal tissue.

IST is microtubule dependent, and MST is actomyosin dependent

We next asked whether interphasic and mitotic translocations were driven by distinct molecular mechanisms or were merely the same process occurring at different speeds. To test this, we first established *in vitro* 2D cultures of fetal RG cells, using fibronectin-coated dishes (Figure 2A). The cells maintained an elongated morphology and were positive for the RG markers SOX2, HOPX, PTPRZ1, and LIFR and negative for EOMES and NEUN (Figures S2A and S2B). These cells still performed IST and MST *in vitro*, indicating that these movements are cell autonomous (Figures 2B–2D). Live imaging of these cells from birth to division revealed an ~2 times shorter cell cycle than in tissues (Figures 2E and S2C). IST velocity was constant during interphase, while MST was much faster, as observed in tissues (Figure 2F). However, both IST and MST were substantially faster, more frequent, and of higher amplitude in 2D dissociated cultures as compared with organoids or fetal tissue, suggesting a negative effect of tissue environment on translocation efficiency (Figures S2D–S2I).

We validated the cell cycle dependency of IST and MST using the fluorescent ubiquitination-based cell cycle indicator (FUCCI) system, which marks G1 cells in red and S/G2 cells in green.[44,45] As expected, IST was equally likely to occur in RFP- and GFP-expressing cells, whereas MST strictly occurred in GFP-expressing cells, just before the loss of the GFP signal at anaphase (Figures S3A–S3D). We confirmed these results using the Cdk1 inhibitor RO-3306, which impairs the G2/M transition. This treatment abolished MST without affecting IST (Figures S3D–S3I).

To investigate the role of the cytoskeleton in IST and MST, we expressed the centrosomal marker Centrin2 in dissociated RG cells. During IST, the centrosome always moved ahead of the nucleus and organized a microtubule cage around the nucleus, consistent with microtubule-dependent pulling forces on the nuclear envelope (Figures 2G and S3J). To test this, as well as the possibility of a role of actomyosin contractility, cells were treated with the microtubule depolymerizing drug nocodazole and the myosin II inhibitor blebbistatin. These experiments revealed that IST was severely affected by microtubule depolymerization but not by actomyosin inhibition (Figures 2H and 2I). Conversely, and as previously published,[19] MST was abolished by myosin II inhibition but not by microtubule depolymerization (Figures 2J and 2K). Consistently, phosphorylated myosin II was observed at the cortex of mitotic RG cells (Figure 2L).

Finally, we asked whether MST occurs before or after nuclear envelope breakdown. To test this, we incubated dissociated RG cells with SiR-Tubulin and performed live imaging. These experiments revealed that the mitotic spindle always formed before MST initiation, indicating that MST is not a nuclear translocation event but a mitotic spindle translocation event occurring during prometaphase-metaphase (Figures 2M and 2N). Overall, these results show that IST is a microtubule-dependent nuclear transport event occurring throughout interphase, while MST is an actomyosin-dependent mitotic spindle translocation event occurring during prometaphase.

Dynein, LIS1, and the LINC complex drive IST in bRG cells

We next addressed the molecular mechanism of IST. We first confirmed that, as in dissociated cultures, nocodazole—but not blebbistatin—impaired IST in cortical organoids (Figure S4A). Because microtubule-dependent nuclear transport is largely dependent on the dynein motor in many cell types, we infected week 8–11 human cortical organoids with dynein heavy chain (DYNC1H1) short hairpin RNA (shRNA)-coding lentiviruses. Live imaging revealed that dynein knockdown (KD) affected the amplitude and frequency of IST, with a 3-fold decrease in the distance travelled over time (Figures 3A, 3C, S4B, and S4C). These results were obtained for two independent and validated shRNA sequences. The role of dynein in IST was confirmed in human fetal tissue in three independent live-imaged samples (pcw 16–20) (Figures 3B and 3E). Dynein loss of function did not affect MST (Figures 3D, 3F, S4D, and S4E). We then knocked down the dynein activator LIS1 in bRG cells. Infection with retroviruses encoding LIS1 shRNA constructs strongly affected IST in live-imaged human cortical organoids, fetal tissue, and dissociated fetal RG cultures (Figures 3A, 3C, 3E, and S4B–S4G). As for dynein, LIS1 KD did not affect MST (Figures 3D, 3F, and S4C–S4E). Mutations in the LIS1 gene are the most prevalent cause of lissencephaly in humans, a disease associated with neuronal positioning defects.[46,47] To test whether bRG cell translocation defects may occur in lissencephalic tissue, we generated LIS1 patient-derived cortical organoids from two affected individuals.[48] Live imaging of bRG cells within these organoids at weeks 8–11 confirmed a strong IST

(J) Live imaging of *in vitro* bRG cells during mitosis, treated with DMSO, nocodazole (1 μM), or blebbistatin (10 μM).
(K) Quantification of MST amplitude following treatment with DMSO, nocodazole (1 μM), or blebbistatin (10 μM) in *in vitro* bRG cells (n = 3 experiments, 724 bRG cells).
(L) Mitotic (condensed chromosomes) human fetal RG cell *in vitro* stained with anti-pMLC2 (phospho-myosin light chain 2), phalloidin, and DAPI.
(M) Live imaging of an *in vitro* bRG cell performing MST and expressing SiR-Tubulin. Mitotic spindle begins to form before translocation.
(N) Quantification of the fraction of bRG cells in which mitotic spindle forms before somal translocation starts (n = 2 experiments, 94 bRG cells).
Yellow arrowheads indicate bRG cell soma, and green and red arrowheads indicate daughter cells.
Data are presented as mean values ± SD. Scale bar, 20 μm. All live imaging montages are in h and min. *$p < 0.05$; **$p < 0.01$; ****$p < 0.0001$; ns: non-significant by two-tailed unpaired t tests.

Please cite this article in press as: Wimmer et al., Two translocation mechanisms drive neural stem cell dissemination into the human fetal cortex, Neuron (2026), https://doi.org/10.1016/j.neuron.2026.02.002

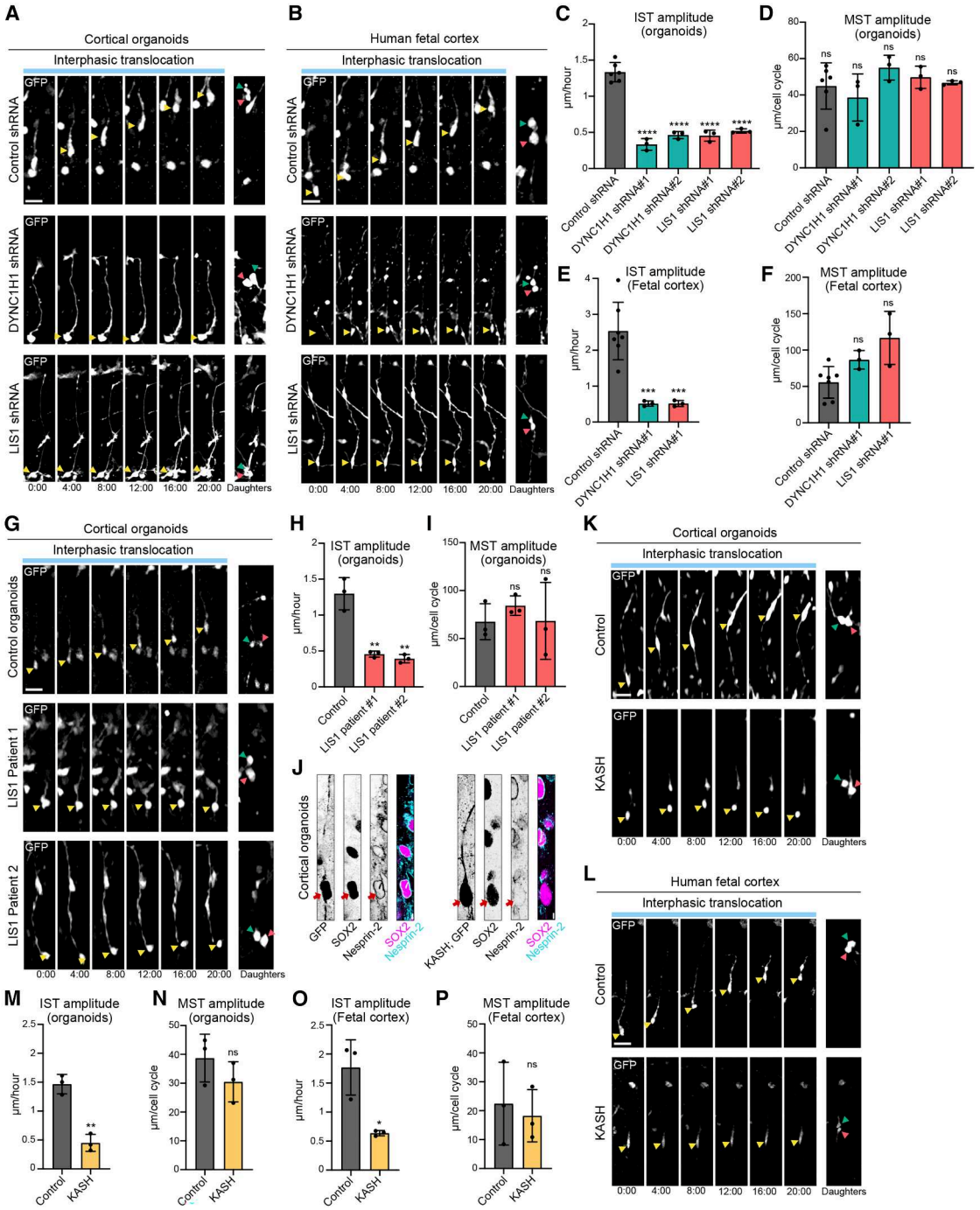

Figure 3. Dynein-LIS1 recruitment to the nuclear envelope by the LINC complex drives IST

(A) Live imaging of interphasic human bRG cells expressing control, DYNC1H1, or LIS1 shRNA constructs in human cortical organoids (weeks 8–11). shRNA plasmids co-express GFP.

(B) Live imaging of interphasic human bRG cells expressing control, DYNC1H1, or LIS1 shRNA constructs in human fetal tissue (pcw 16–18).

(C) Quantification of IST amplitude in human bRG cells expressing control, DYNC1H1, or LIS1 shRNA constructs in human cortical organoids (n = 3 organoid batches, 899 bRG cells, weeks 8–11). Two independent shRNA plasmids were used for each knockdown.

(D) Quantification of MST amplitude in human bRG cells expressing control, DYNC1H1, or LIS1 shRNA constructs in human cortical organoids (n = 3 organoid batches, 899 bRG cells, weeks 8–11).

(E) Quantification of IST amplitude in human bRG cells expressing control, DYNC1H1, or LIS1 shRNA constructs in human fetal tissue (n = 3 fetal samples, 385 bRG cells, pcw 16–20).

(legend continued on next page)

Please cite this article in press as: Wimmer et al., Two translocation mechanisms drive neural stem cell dissemination into the human fetal cortex, Neuron (2026), https://doi.org/10.1016/j.neuron.2026.02.002

alteration without any MST defect (Figures 3G–3I, S4H, and S4I). Therefore, dynein and its activator LIS1 control nucleokinesis during IST in bRG cells.

We then asked how the dynein-LIS1 motor complex was targeted to the nuclear envelope of bRG cells. Because IST occurred with a leading centrosome and throughout interphase, we hypothesized that it worked through a mechanism similar to the linker of nucleoskeleton and cytoskeleton (LINC) complex-dependent nuclear translocation in migrating neurons, but different from the nuclear pore-dependent INM in aRG cells.[49] To test this, we expressed the KASH domain of Nesprin-2, which acts as a dominant negative by displacing all Nesprins from the nuclear envelope.[50] This construct efficiently displaced Nesprin-2 from the nuclear envelope of bRG cells in cortical organoids (Figure 3J). Live imaging revealed that KASH expression severely altered IST in human cortical organoids, fetal tissue, and fetal RG *in vitro* cultures, without any effect on MST (Figures 3K–3P and S4J–S4L). For all these conditions, we noted that IST was affected but not abolished. We therefore wondered whether actomyosin contractility could be taking over to support partial movement. To test this, we incubated KASH-expressing *in vitro* bRG cells with blebbistatin. This, however, did not increase the IST phenotype, further indicating that IST is actomyosin-independent (Figure S4J).

Finally, we tested whether dynein was indeed the downstream target of Nesprins at the nuclear envelope. To do so, we fused the Nesprin KASH motif to the N-terminal domain of the dynein/dynactin adaptor BicD2. As previously reported in other cell types,[51] we observed a strong recruitment of dynactin at the nuclear envelope of human fetal RG cells expressing this construct (Figure S4M). We next live-imaged fetal RG expressing the KASH dominant-negative (which displaces endogenous Nesprins) and the N-BicD2-KASH construct (in which the dynein/dynactin complex is recruited in the absence of endogenous Nesprins). This experiment revealed that the IST defects observed in KASH-expressing cells were almost completely rescued by the N-BicD2-KASH construct, indicating that Nesprins indeed act through the dynein motor for IST movement (Figures S4N and S4O). Overall, these experiments show that IST is driven by dynein-LIS1 pulling forces, which are recruited to the nuclear envelope by the LINC complex (see Figure 5H for a model).

Mitotic cell rounding drives MST in bRG cells

Most cells round up in mitosis to enable proper chromosome segregation through a process known as mitotic cell rounding.[52] This process occurs via mitotic phosphorylation of the RhoGEF Ect2 by Cdk1, which activates RhoA to trigger actomyosin contractility, and by mitotic phosphorylation of the ezrin-radixin-moesin (ERM) proteins, which crosslink the actin cortex to the plasma membrane.[53–55] A vimentin layer beneath the actin cortex further increases mitotic cortical tension (see Figure 5H for a model).[56,57] We hypothesized here that this mitotic cortical tension is the force driving translocation of the bRG cell soma. To test for the role of mitotic cell rounding in MST, we first knocked down, one by one, the members of the ERM family, as well as vimentin, in fetal RG cultures using shRNA constructs. KD of moesin and radixin strongly reduced the average amplitude of MST, without affecting IST, while KD of ezrin had a milder effect (Figures 4A and 4B). KD of vimentin phenocopied moesin and radixin loss of function, impairing proper MST in these cells (Figures 4A and 4B).

We next tested whether activation of this pathway would be sufficient to trigger MST outside of mitosis. In HeLa cells, deadhesion using Accutase treatment induces phosphorylation of the ERM proteins and cell rounding during interphase.[58] Likewise, treatment of fetal RG cultures with Accutase led to a fast and massive ERM phosphorylation in non-mitotic RG cells, as well as cell rounding (Figures 4C–4E). This treatment did not affect the number of mitotic cells (Figure 4F). Live imaging revealed that 60% of Accutase-treated fetal RG cells underwent fast MST-like behavior within 10 min of treatment (Figures 4G and 4H). These cells were largely interphasic because they did not end up dividing within the next 2 h, and only 4% of fetal RG cells are in mitosis at a given time (Figure 4F). Translocation

(F) Quantification of MST amplitude in human bRG cells expressing control, DYNC1H1, or LIS1 shRNA constructs in human fetal tissue ($n = 3$ fetal samples, 385 bRG cells, pcw 16–20).
(G) Live imaging of interphasic human bRG cells expressing GFP in control cortical organoids and two different patient-derived LIS1-mutated organoids (weeks 8–11).
(H) Quantification of IST amplitude in control cortical organoids and two different patient-derived LIS1-mutated organoids ($n = 3$ organoid batches, 397 bRG cells, weeks 8–11).
(I) Quantification of MST amplitude in control cortical organoids and two different patient-derived LIS1-mutated organoids ($n = 3$ organoid batches, 397 bRG cells, weeks 8–11).
(J) Immunostaining for SOX2 and Nesprin-2 in cortical organoids expressing GFP or the KASH dominant negative together with GFP (week 9). Red arrows indicate the nuclear envelope of construct-expressing cells.
(K) Live imaging of interphasic human bRG cells expressing control or KASH constructs in human cortical organoids (week 8). KASH plasmid co-expresses GFP.
(L) Live imaging of interphasic human bRG cells expressing control or KASH constructs in human fetal tissue (pcw 16). KASH plasmid co-expresses GFP.
(M) Quantification of IST amplitude in human bRG cells expressing control or KASH constructs in human cortical organoids ($n = 3$ organoid batches, weeks 8–11, 201 bRG cells).
(N) Quantification of MST amplitude in human bRG cells expressing control or KASH constructs in human cortical organoids ($n = 3$ organoid batches, weeks 8–11, 201 bRG cells).
(O) Quantification of IST amplitude in human bRG cells expressing control or KASH constructs in human fetal tissue ($N = 3$ fetal samples, pcw 16–18, 97 bRG cells).
(P) Quantification of MST amplitude in human bRG cells expressing control or KASH constructs in human fetal tissue ($N = 3$ fetal samples, pcw 16–18, 97 bRG cells).
Yellow arrowheads indicate bRG cell soma, and green and red arrowheads indicate daughter cells. Data are presented as mean values ± SD. Scale bar, 20 μm. All live imaging montages are in h and min. $^{*}p < 0.05$; $^{**}p < 0.01$; $^{****}p < 0.0001$, ns: non-significant by two-tailed unpaired *t* tests.

Please cite this article in press as: Wimmer et al., Two translocation mechanisms drive neural stem cell dissemination into the human fetal cortex, Neuron (2026), https://doi.org/10.1016/j.neuron.2026.02.002

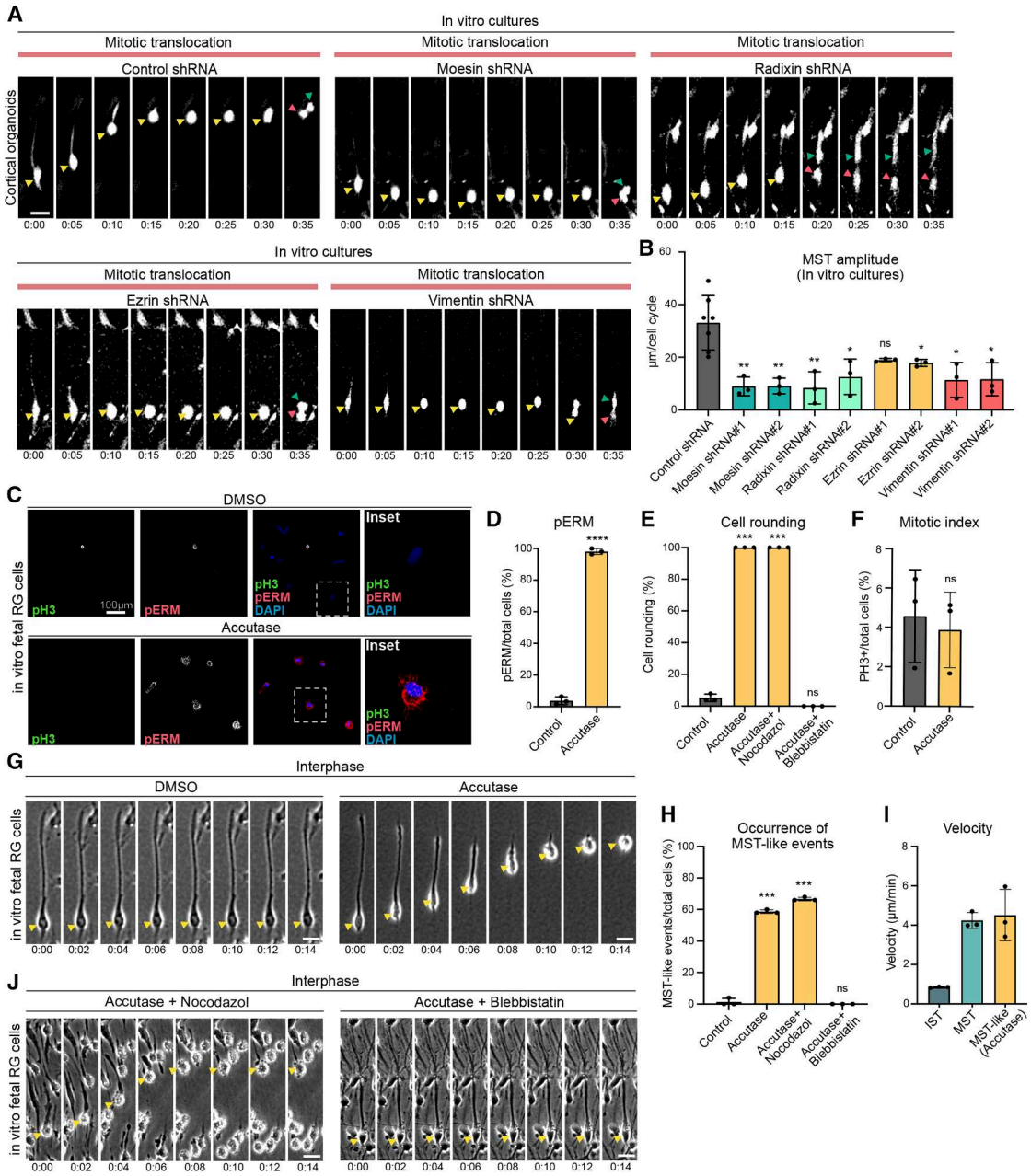

Figure 4. Mitotic cell rounding drives mitotic somal translocation in fetal RG cells *in vitro*

(A) Live imaging of *in vitro* mitotic human bRG cells expressing control, moesin, radixin, ezrin, or vimentin shRNA constructs.

(B) Quantification of IST amplitude in *in vitro* interphasic human bRG cells expressing control, moesin, radixin, ezrin, or vimentin shRNA constructs. Two independent shRNA plasmids were used for each knockdown (N = 7 control samples and n = 3 samples per shRNA condition, 522 bRG cells).

(C) Human fetal RG cell *in vitro* immunostained for pH3, pERM, and marked for DAPI following 15 min Accutase treatment. Dotted rectangles indicate inset.

(D) Quantification of pERM+ cells out of total fetal RG cells following 15 min Accutase treatment (n = 3 independent experiments, 215 cells).

(E) Quantification of the percentage of rounded fetal RG cells following 15 min Accutase, Accutase + Nocodazole, or Accutase + blebbistatin treatment (n = 3 independent experiments, 215 cells).

(F) Quantification of pH3+ cells out of total fetal RG cells following 15 min Accutase treatment (n = 3 independent experiments, 3,449 cells).

(G) Live imaging of fetal RG cell *in vitro* during interphase following Accutase treatment.

(H) Quantification of the occurrence of MST-like events in fetal RG cells treated with Accutase, Accutase + Nocodazole, or Accutase + blebbistatin (n = 3 independent experiments, 600 cells).

(I) Quantification of the velocity of IST, MST, and MST-like events (Accutase) in fetal RG cells (n = 3 independent experiments, 600 cells).

(legend continued on next page)

Please cite this article in press as: Wimmer et al., Two translocation mechanisms drive neural stem cell dissemination into the human fetal cortex, Neuron (2026), https://doi.org/10.1016/j.neuron.2026.02.002

speed of Accutase-treated cells was identical to that of MST and much higher than IST (Figure 4I). Moreover, this MST-like movement was insensitive to nocodazole treatment but completely inhibited by blebbistatin (Figures 4H and 4J). Therefore, forced deadhesion of fetal RG cells leads to ERM phosphorylation, cell rounding, and fast actomyosin-dependent MST-like movement during interphase.

We then asked whether the roles of moesin and vimentin were maintained in 3D samples. KD of moesin and vimentin in week 8–12 cortical organoids severely altered MST without affecting IST (Figures 5A, 5C, 5D, S5A, and S5B). Likewise, moesin and vimentin KDs in multiple independent human fetal samples severely disrupted MST without affecting IST (Figures 5B, 5E, and 5F). Consistently, ERM phosphorylation was detected at the cortex of mitotic bRG cells (Figure 5G). These results identify mitotic cell rounding as the driver of MST in human bRG cells (Figure 5H).

We observed that factors altering IST did not affect MST and all factors altering MST did not affect IST. To further test for the interdependence of the two translocation processes, we asked whether, in non-perturbed conditions, the occurrence of one of them influenced the likelihood of the other to occur. Strikingly, we observed that IST is more likely to occur if MST does not occur afterward, and MST is more likely to occur if IST did not occur before (Figures S5C and S5D).

Finally, we tested whether inhibition of the factors controlling IST and MST affected bRG cell mitosis and progression in the cell cycle. Impairment of IST and MST using KASH dominant negative and moesin KD did not alter bRG cell mitotic spindle orientation, nor did it affect the ventricular lining (Figures S5E and S5F). Loss of function of MST proteins (moesin and vimentin) did not alter bRG cell mitotic index (Figures S5G and S5H). Inhibition of IST factors gave mixed results due to the well-known function of some of them in mitosis. Inhibition of nesprin—which has no major mitotic function—did not alter bRG cell mitotic index, whereas inhibition of dynein and Lis1 (and Lis1 patient organoids) increased mitotic index due to their mitotic spindle assembly roles[59] (Figures S5G and S5H). Ki67 index was not affected as cells delayed in mitosis remain in the cell cycle (Figures S5G and S5I). Therefore, impairment of IST and MST per se does not alter cell cycle progression, but many IST factors do due to their IST-independent mitotic roles.

IST contributes more than MST to bRG cellcolonization of the human fetal neocortex

Next, we measured the relative contribution of interphasic and mitotic translocations to bRG cell colonization of the human developing neocortex. The average amplitude of IST and MST movement in fetal tissue, throughout an entire cell cycle and including the static cells, was 77 and 20.4 μm, respectively, indicating that IST leads to 3.7× more movement of the bRG cell soma than MST (Figure 6A). A similar bias for IST was observed in cortical organoids, albeit smaller (1.7×), because MST was higher and IST slightly lower than in fetal tissues (Figure 6A).

A second factor influencing the contribution of IST and MST to bRG cell colonization of the human cortex is their directionality. As previously reported for MST,[22,35] we found both IST and MST to be bidirectional, occurring in the apical and basal directions, in human fetal tissue and cortical organoids (Figures 6B–6E). Translocation was apical in cells with an apical process and basal in cells with a basal process (Figure S6A). When cells were bipolar, IST and MST generally occurred in the thicker process (Figure S6B). Quantification of directionality in human fetal tissues revealed that IST and MST were both biased toward the basal side (Figures 6F and 6G). IST was slightly more polarized than MST (2.2 vs. 1.7 basal bias, respectively). In organoids, MST showed a much stronger basal bias than IST (6.6 vs. 2.2 basal bias, respectively) (Figures 6H and 6I). Whether cells translocated apically or basally, they did so with similar amplitudes in fetal tissues and in organoids (Figures 6J–6M). IST and MST perturbations did not affect their directionality, with defects in apical and basal translocations following DYNC1H1 or moesin shRNA (Figure S6C). Together, these results show that IST and MST are both biased toward the basal side in the fetal cortex. This basal polarity comes from the higher frequency—not amplitude—of basal translocation events, which is a direct consequence of bRG cell shapes.

We next integrated all these results to quantify how much IST and MST contributed to basal dissemination of bRG cells, considering their respective frequency, directionality, and amplitude. In human fetal tissues, bRG cells progressed basally by 155 μm per week of gestation (Figure 6N). IST was the strongest contributor to this movement, accounting for 130 μm of movement, while MST only accounted for 25 μm. Therefore, IST contributes to 85% of the total basal translocation of bRG cells in the human developing neocortex. This difference is largely due to the greater amplitude of movement of IST, which occurs throughout the 46 h cell cycle, rather than to its biased polarity. The contribution of IST and MST to basal displacement remained relatively constant from pcw 12 to 19 (Figure S6E). In cortical organoids, the total net basal displacement of bRG cells was similar to that of fetal tissues (135 μm per week) (Figure 6N). However, unlike in fetal tissue, MST was the strongest contributor to bRG cell basal displacement, representing 66% of the total.

To confirm the role of IST and MST in the basal dissemination of bRG cells, we analyzed the long-term consequence of their impairment. Fetal cortex explants were electroporated from the ventricular surface and cultivated for 3 weeks. We observed a strong alteration in the basal dissemination of KASH-expressing cells and a milder effect in moesin shRNA-expressing cells, consistent with the stronger contribution of IST to basal displacement of bRG cells (Figures 6O, 6P, and S6F).

Finally, we asked whether the translocation characteristics of bRG cells were different depending on their position along the

(J) Live imaging of fetal RG cells *in vitro* during interphase following Accutase + Nocodazole or Accutase + blebbistatin treatment.
Yellow arrowheads indicate bRG cell soma, and green and red arrowheads indicate daughter cells.
Data are presented as mean values ± SD. Scale bar, 20 μm. All live imaging montages are in h and min. *$p < 0.05$; **$p < 0.01$; ***$p < 0.001$; ****$p < 0.0001$; ns: non-significant by two-tailed unpaired *t* tests.

Please cite this article in press as: Wimmer et al., Two translocation mechanisms drive neural stem cell dissemination into the human fetal cortex, Neuron (2026), https://doi.org/10.1016/j.neuron.2026.02.002

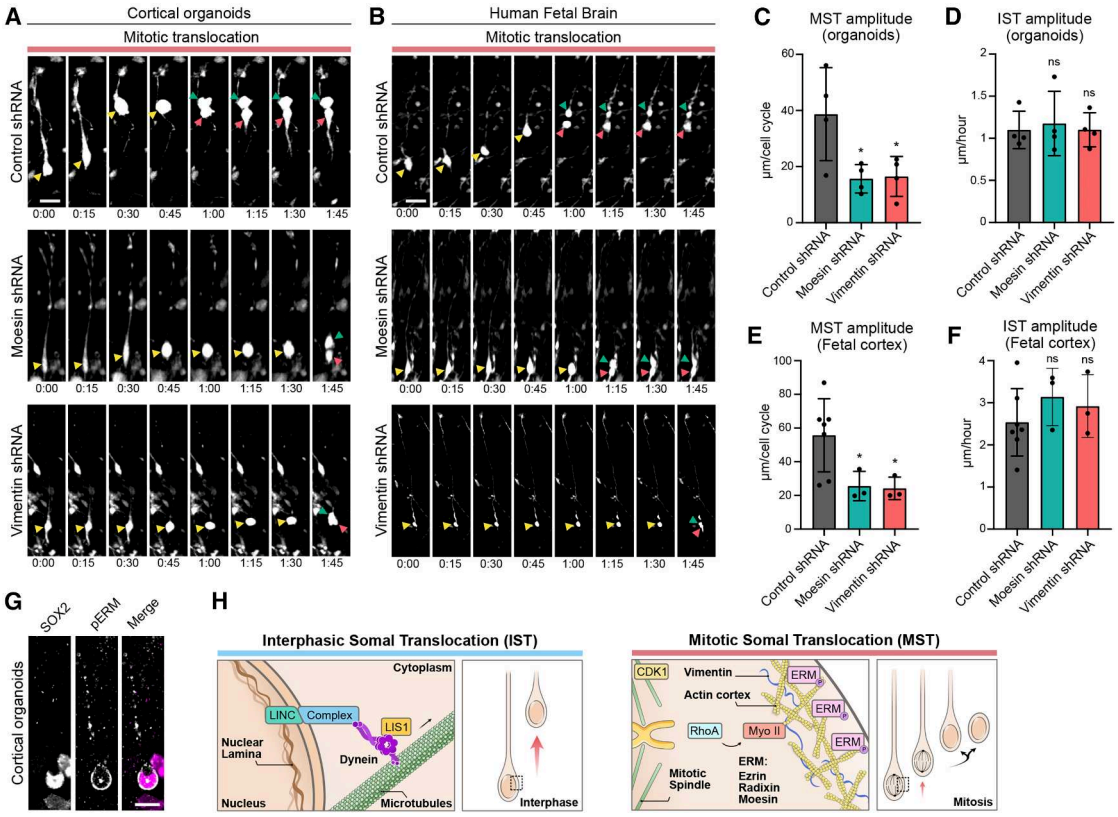

Figure 5. Mitotic cell rounding drives mitotic somal translocation in organoids and fetal cortex

(A) Live imaging of mitotic human bRG cells expressing control, moesin, or vimentin shRNA constructs in human cortical organoids (week 9).

(B) Live imaging of mitotic human bRG cells expressing control, moesin, or vimentin shRNA constructs in human fetal tissue (pcw 20).

(C) Quantification of MST amplitude in human bRG cells expressing control, moesin, or vimentin shRNA constructs in human cortical organoids (n = 4 organoid batches, 453 bRG cells, weeks 8–12).

(D) Quantification of IST amplitude in human bRG cells expressing control, moesin, or vimentin shRNA constructs in human cortical organoids (n = 4 organoid batches, 453 bRG cells, weeks 8–12).

(E) Quantification of MST amplitude in human bRG cells expressing control, moesin, or vimentin shRNA constructs in human fetal tissue (n = 7 fetal samples, 568 bRG cells, pcw 14–20).

(F) Quantification of IST amplitude in human bRG cells expressing control, moesin, or vimentin shRNA constructs in human fetal tissue (n = 7 fetal samples, 568 bRG cells, pcw 14–20).

(G) Immunostaining for SOX2 and pERM in mitotic bRG cells from week 8 cortical organoid.

(H) Schematic representation of the molecular mechanisms driving IST and MST.

Yellow arrowheads indicate bRG cell soma, and green and red arrowheads indicate daughter cells.

Data are presented as mean values ± SD. Scale bar, 20 µm. All live imaging montages are in h and min. *$p < 0.05$, ns: non-significant by two-tailed unpaired t tests.

apico-basal axis of the human fetal cortex. We separated the oSVZ into two equal parts, defining a lower and an upper oSVZ (below and above 1.5 mm from the ventricle) (Figure 6Q). Cells in the lower oSVZ relied less on IST and more on MST than cells in the upper oSVZ (Figure 6R). In this regard, bRG cells in organoids, which have a small oSVZ, are similar to bRG cells in the lower region of the human fetal oSVZ. This may explain why IST and MST directionally are slightly different between organoids and fetal tissue. Overall, these results show that IST contributes 5.5 times more than MST to basal dissemination of bRG cells in the developing human fetal cortex.

IST and MST occur in glioblastoma cells

The presence of embryonic bRG-like cells has been reported within adult glioblastoma samples.[60,61] These cells were proposed to act as a cancer stem cell-like pool through reactivation or maintenance of their developmental program. Notably, these cells maintain MST, further validating the parallels between bRG cells and this population of glioblastoma (GBM) cells.[60] We therefore asked whether glioblastoma cells also underwent IST, and whether the molecular mechanisms that we uncovered here for IST and MST also act in these cells. Because GBMs are highly heterogeneous in cell composition,[62] we live-imaged a panel of 9 different glioblastoma lines maintained under neural stem cell culture conditions and scored for the ones where IST or MST were seen in more than 10% of the cells.[63] The analysis confirmed heterogeneity and revealed that 5 out of 9 lines performed IST, whereas 4 out of 9 lines performed MST (Figures 7A–7D). Notably, line U3123 displayed frequencies of IST and MST extremely similar to those of bRG cells *in vitro*.

Please cite this article in press as: Wimmer et al., Two translocation mechanisms drive neural stem cell dissemination into the human fetal cortex, Neuron (2026), https://doi.org/10.1016/j.neuron.2026.02.002

CellPress
OPEN ACCESS

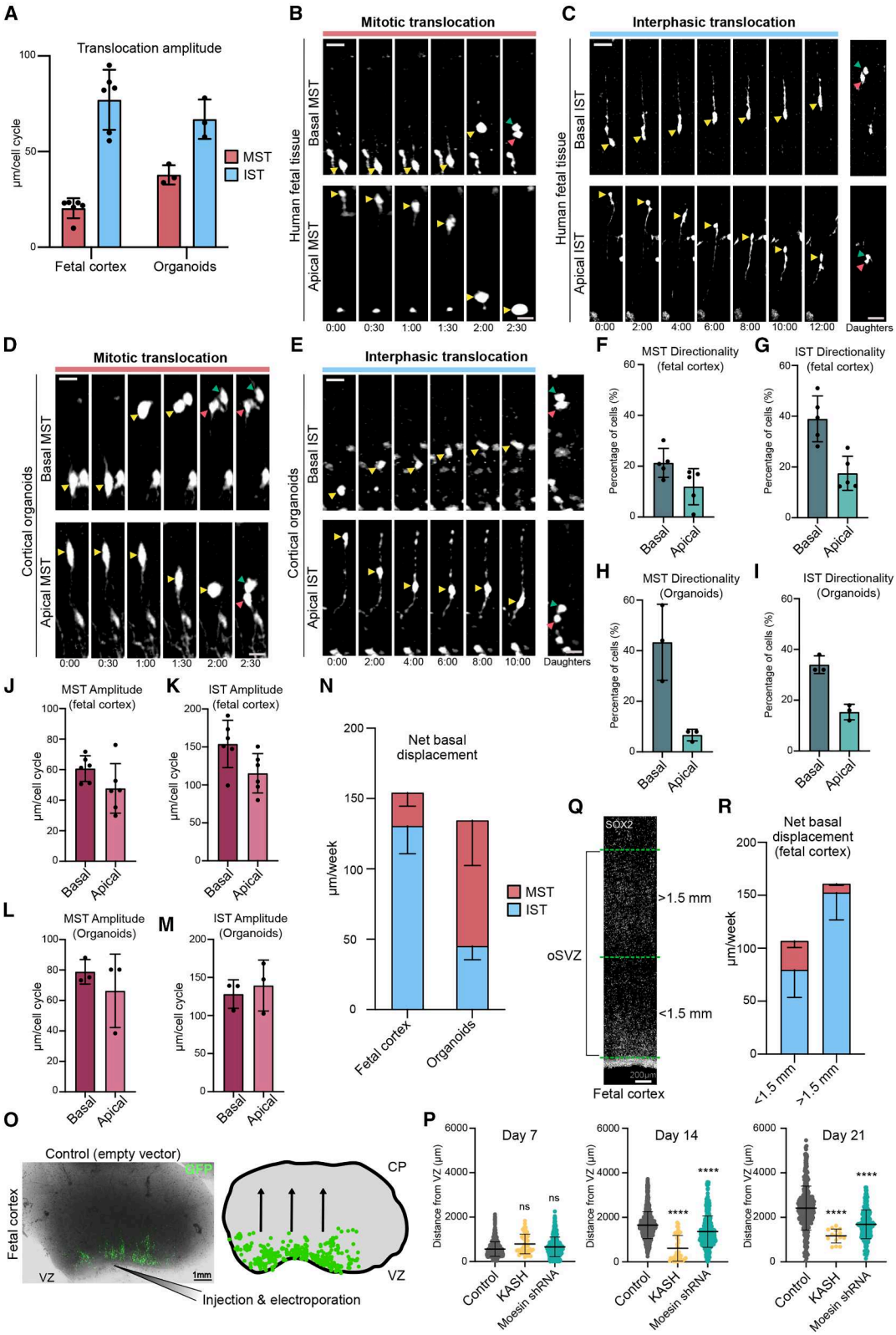

(legend on next page)

Please cite this article in press as: Wimmer et al., Two translocation mechanisms drive neural stem cell dissemination into the human fetal cortex, Neuron (2026), https://doi.org/10.1016/j.neuron.2026.02.002

These cells were furthermore positive for the RG cell markers SOX2 and HOPX (Figure 6E). We asked whether bRG-like identity could be a marker of cells undergoing IST and MST. The glioblastoma transcriptome revealed that these lines indeed had a strong RG identity, but no correlation between individual line proximity to RG and IST/MST occurrence was observed (Figures S7A and S7B). Overall, these results indicate that IST and MST heterogeneously occur in glioblastoma cells.

We next used line U3123 to test whether the molecular mechanisms of IST and MST were maintained in GBM cells. Incubation of U3123 with nocodazole completely abolished IST, whereas blebbistatin had no effect (Figures 7F and 7G). Conversely, incubation with blebbistatin completely abolished MST, whereas nocodazole had no effect (Figures 7H and 7I). Therefore, as for bRG cells, IST is microtubule dependent and MST is actomyosin dependent in GBM cells. We then asked whether the underlying molecular mechanisms for both movements were identical. shRNA-mediated KD of LIS1 indeed altered IST without affecting MST in GBM cells (Figures 7J and 7K). Likewise, expression of the LINC complex dominant negative KASH construct reduced IST in these cells (Figures 7J and 7L). Conversely, KD of moesin and vimentin in GBM cells impaired MST without affecting IST (Figures 7M and 7N). Together, these results indicate that the molecular mechanisms of IST and MST are identical in fetal bRG cells and GBM cells.

DISCUSSION

Our work provides a descriptive and mechanistic study of bRG cell colonization of the human fetal neocortex. We identify two distinct modes of translocation: IST, occurring in interphase in a microtubule-dependent manner, and MST, occurring during mitosis, relying on the actin cytoskeleton. We demonstrate that IST is controlled by dynein and its activator LIS1, which are recruited to the nuclear envelope by the LINC complex, whereas MST is driven by the mitotic cell-rounding pathway through ERM proteins as well as vimentin and actomyosin contractility. IST contributes five times more than MST to the dissemination of bRG cells in the human fetal cortex, resulting in a total movement of 0.67 mm per month of gestation. We furthermore show that IST is altered in lissencephalic patients and that bRG-like glioblastoma cells also utilize IST and MST for their movement. This work therefore identifies the molecular mechanism underlying neural stem cell colonization of the human fetal cortex, with important implications in pathological contexts.

Similar to apical nuclear migration in aRG cells and nucleokinesis in migrating neurons, IST in bRG cells depends on the dynein motor. We show here that the LINC complex-dependent pathway for dynein recruitment to the nuclear envelope is the same as in neurons but different from aRG cells, where dynein is recruited to the nuclear pore complex.[49,64–66] Therefore, IST is molecularly closer to neuronal migration than it is to INM, even though bRG cells are transcriptionally much closer to aRG cells than to neurons.[67,68] This is likely because apical nuclear migration in aRG cells is a G2-specific mechanism, while IST and neuronal migration are not. A notable difference between neurons and bRG cells is that neuronal migration is dependent on actomyosin, whereas IST is not. This may reflect a prevalent role for actomyosin in neuronal leading-edge progression, while bRG cells have pre-extended static processes that do not need to grow during translocation.

We show that MST is a mitotic spindle translocation event that occurs after nuclear envelope breakdown and is driven by the process of mitotic cell rounding. This well-described pathway induces an important stiffening of the cell cortex, enabling

Figure 6. IST contributes more than MST to bRG cell colonization of the human fetal neocortex

(A) Quantification of the amplitude of IST and MST in human fetal tissue (N = 5 fetal samples, 476 bRG cells, pcw 12–19; n = 3 organoid batches, 150 bRG cells, weeks 7–9).
(B) Live imaging of human bRG cells expressing GFP, performing apically or basally directed MST in human fetal tissue (pcw 14).
(C) Live imaging of human bRG cells expressing GFP, performing apically or basally directed IST in human fetal tissue (pcw 14).
(D) Live imaging of human bRG cells expressing GFP, performing apically or basally directed MST in human cortical organoids (week 8).
(E) Live imaging of human bRG cells expressing GFP, performing apically or basally directed IST in human cortical organoids (week 8).
(F) Quantification of the directionality of MST in human fetal tissue (n = 5 fetal samples, 476 bRG cells, pcw 12–19).
(G) Quantification of the directionality of IST in human fetal tissue (n = 5 fetal samples, 476 bRG cells, pcw 12–19).
(H) Quantification of the directionality of MST in human cortical organoids (n = 3 organoid batches, 150 bRG cells, week 7–9).
(I) Quantification of the directionality of IST in human cortical organoids (n = 3 organoid batches, 150 bRG cells, week 7–9).
(J) Quantification of the amplitude of MST, depending on directionality, in human fetal tissue (n = 5 fetal samples, 476 bRG cells, pcw 12–19).
(K) Quantification of the amplitude of IST, depending on directionality, in human fetal tissue (n = 5 fetal samples, 476 bRG cells, pcw 12–19).
(L) Quantification of the amplitude of MST, depending on directionality, in human cortical organoids (n = 3 organoid batches, 150 bRG cells, week 7–9).
(M) Quantification of the amplitude of IST, depending on directionality, in human cortical organoids (n = 3 organoid batches, 150 bRG cells, week 7–9).
(N) Contribution of MST and IST to the total net basal displacement of bRG cells in human fetal tissue and in human cortical organoids (n = 5 fetal samples, 476 bRG cells, pcw 12–19; n = 3 organoid batches, 150 bRG cells, week 7–9).
(O) Electroporation of pcw 17 human fetal tissue from the ventricular surface with GFP empty vector, imaged at day 7 of slice culture. CP, cortical plate; VZ, ventricular zone.
(P) Quantification of GFP+ cell distance from the VZ in control vector-, KASH dominant-negative-, and moesin shRNA-expressing cells at day 7, 14, and 21 of slice culture in pcw 17 human fetal tissue (n = 3 fetal samples, 10,016 GFP+ cells).
(Q) SOX2 immunostaining of human fetal cortical slices at pcw 15. The apical region and the basal regions of the oSVZ have been separated by a yellow line 1.5 mm from the ventricular surface.
(R) Contribution of MST and IST to the total net basal displacement of bRG cells in human fetal tissue in the apical and basal oSVZ (above and below 1.5 mm from the ventricular surface) (n = 2 fetal samples, 260 bRG cells, pcw 15–19).
Yellow arrowheads indicate bRG cell soma, and green and red arrowheads indicate daughter cells. Data are presented as mean values ± SD. Scale bar, 20 μm. All live imaging montages are in h and min. **** $p < 0.01$; ns: non-significant by two-tailed unpaired t tests.

Please cite this article in press as: Wimmer et al., Two translocation mechanisms drive neural stem cell dissemination into the human fetal cortex, Neuron (2026), https://doi.org/10.1016/j.neuron.2026.02.002

CellPress
OPEN ACCESS

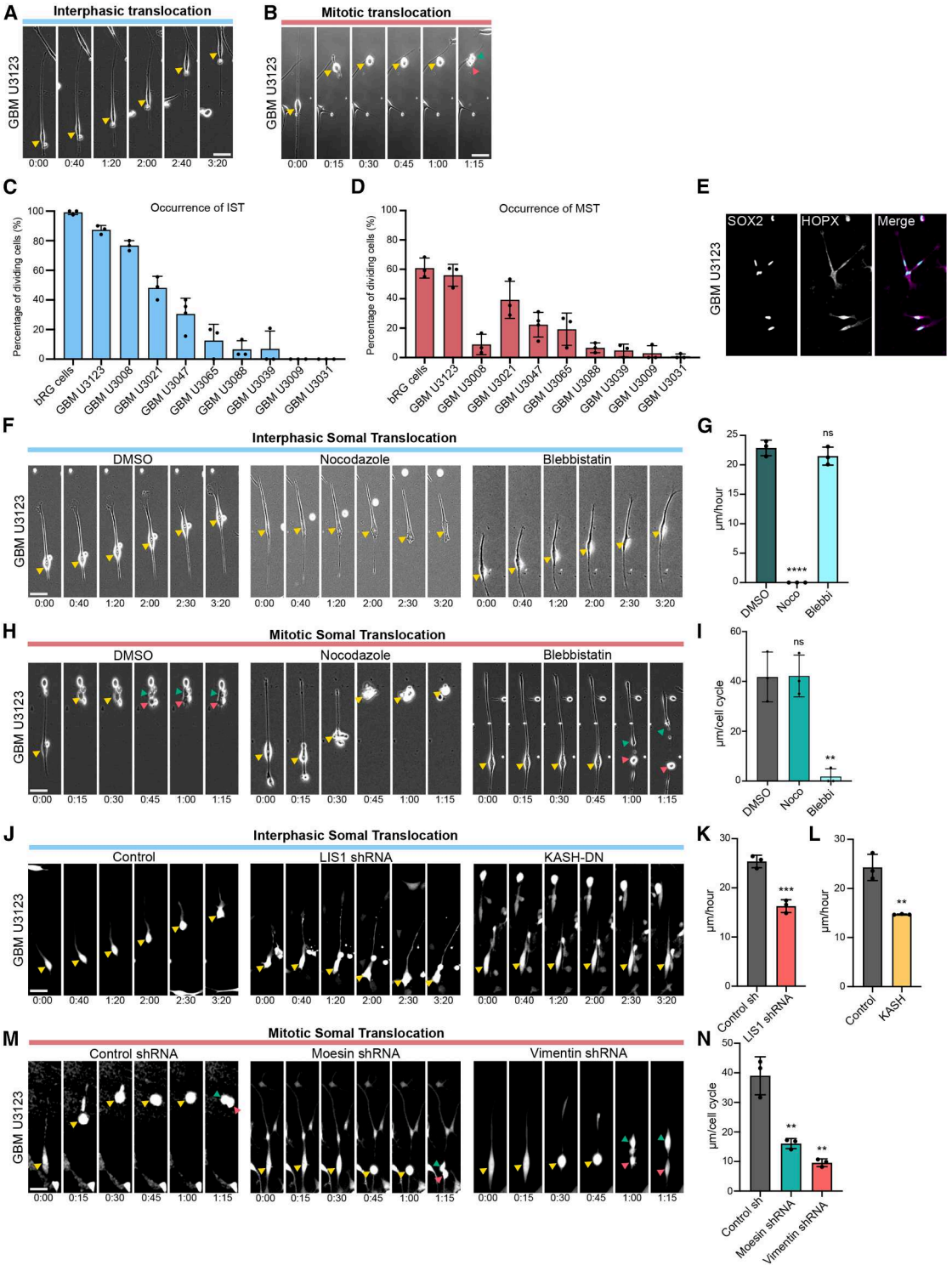

Figure 7. IST and MST also occur in glioblastoma cells

(A) Live imaging of an *in vitro* GBM cell (line U3123) performing IST.

(B) Live imaging of an *in vitro* GBM cell (line U3123) performing MST.

(C) Quantification of the fraction of cells performing IST in 9 GBM lines and in comparison with *in vitro* bRG cells (n = 3 replicates per line, 1,130 cells).

(D) Quantification of the fraction of cells performing MST in 9 GBM lines and in comparison with *in vitro* bRG cells (n = 3 replicates per line, 1,130 cells).

(E) Immunostaining for bRG markers SOX2 and HOPX in the U3123 GBM line.

(legend continued on next page)

Please cite this article in press as: Wimmer et al., Two translocation mechanisms drive neural stem cell dissemination into the human fetal cortex, Neuron (2026), https://doi.org/10.1016/j.neuron.2026.02.002

adherent cells to round up for proper chromosomal segregation. RhoA-ROCK-Myosin II, the ERM proteins (which crosslink the actomyosin network to the plasma membrane), and vimentin (which underlies the actin network and increases stiffness) all participate in MST. Mitotic cell rounding is therefore the force that drives MST, and we propose that two phenomena transform this force into somal movement. First, focal adhesions are destabilized in the soma, a phenomenon well-known to occur during mitotic cell rounding, which releases the soma from the extracellular matrix (ECM). Second, the large intracellular tension that builds up in the soma is dissipated into the basal process of bRG cells, which leads to its engulfment and translocation. Why some cells do not perform MST and remain static is unclear, but this may be due to incomplete focal adhesion disassembly or reduced intracellular tension.

We show here that IST and MST rely on different molecular machineries and that they have additive effects, together enabling bRG cells to translocate basally. It remains to be determined whether IST and MST are entirely independent processes. We show that inhibition of one process does not affect the other, indicating the absence of a sensing mechanism that would compensate for alteration of one of the modes. Nevertheless, in the absence of perturbation, cells are less likely to undergo MST if they did not undergo IST, and vice versa, suggesting a common upstream regulation for IST and MST. Accordingly, although we observe that the relative contributions of IST and MST are different between organoids and fetal tissue, their additive displacement is very similar in the two systems.

Although bRG cell translocation is the mechanism by which they colonize the neocortex, the actual role of this process remains unclear. Our results indicate that IST and MST are not required for cell cycle progression of bRG cells, but they may regulate their output. bRG cells were indeed shown to undergo more direct or indirect divisions depending on their apicobasal position within the tissue, so a role for IST and MST may be to position bRG cells into different microenvironments that would influence their output.[22] This question is, however, highly challenging to address, as differences in cell fate decisions are observed between regions distant by hundreds of μm, which bRG cells take weeks to cover in the fetal cortex.

bRG cell translocation might also contribute to neuronal positioning. We indeed show here that, as neurogenesis progresses, bRG cells advance more and more basally into the neocortex. Consequently, they generate newborn neurons further and further away from the ventricular surface. This reduces the distance neurons must travel to reach the top of the cortical plate, as compared with neurons born from aRG cells. In this regard, it is interesting to note that the pathway controlling IST and neuronal migration is largely the same and that loss of function of the underlying gene, for example, dynein, will affect both bRG translocation and neuronal migration. The neuronal positioning phenotype associated with these factors must therefore be seen as the addition of bRG cell and neuronal defects. This is particularly relevant in the case of lissencephaly, a neuronal positioning disease. We show here that in LIS1-mutated patient organoids, IST is severely affected. In these patients, neurons will therefore be born farther away from their final location, amplifying the neuronal migration defects.

A last possible function for bRG cell somal translocation could be to avoid the jamming of these cells. bRG cells indeed have a very high self-amplification capacity, leading to their rapid expansion between weeks 12 and 20 of human fetal gestation.[22] Massive amounts of bRG cells might therefore accumulate in the same location, close to the ventricles where they are born. We speculate that alteration of their ability to translocate could lead to heterotopias, which are abnormal clusters of cells that end up in the white matter postnatally. Bi-directional movement of bRG cells may further enable them to escape clogging. Genes associated with heterotopia are strongly associated with the cytoskeleton, including actin-related genes—such as FLNA—that may affect MST, and microtubule-related genes—such as MAP1B—that may affect IST.

We show here that bRG cells translocate bidirectionally, resulting in a net basal displacement of 0.67 mm per month of human fetal gestation. On top of this active motion, a passive displacement of bRG cells will also occur as a consequence of cell proliferation and tissue growth. Indeed, as bRG cells actively translocate, they expand the oSVZ size and displace its basal boundary. The massive proliferation between these basal cells and the ventricular surface will further push them away, increasing their displacement. Therefore, the combination of oSVZ proliferation and somal translocation together accounts for the total basal displacement of bRG cells. Our work provides a mechanistic understanding of oSVZ growth during human fetal development, a core feature of neocortical expansion during

(F) Live imaging of the U3123 GBM line during interphase, treated with DMSO, nocodazole (1 μM), or blebbistatin (10 μM).
(G) Quantification of IST amplitude following treatment with DMSO, nocodazole (1 μM), or blebbistatin (10 μM) in the U3123 GBM line (n = 3 experiments, 274 GBM cells).
(H) Live imaging of U3123 GBM line during mitosis, treated with DMSO, nocodazole (1 μM), or blebbistatin (10 μM).
(I) Quantification of MST amplitude following treatment with DMSO, nocodazole (1 μM), or blebbistatin (10 μM) in the U3123 GBM line (n = 3 experiments, 274 GBM cells).
(J) Live imaging of interphasic U3123 GBM cells expressing control, LIS1 shRNA, or KASH dominant negative constructs.
(K) Quantification of IST amplitude in the U3123 GBM cells expressing control or LIS1 shRNA constructs (n = 3 experiments, 359 GBM cells).
(L) Quantification of IST amplitude in the U3123 GBM cells expressing control or KASH dominant negative constructs (n = 3 experiments, 300 GBM cells).
(M) Live imaging of mitotic U3123 GBM cells expressing control, moesin, or vimentin shRNA constructs.
(N) Quantification of MST amplitude in U3123 GBM cells expressing control, moesin, or vimentin shRNA (n = 3 experiments, 149 GBM cells).
Yellow arrowheads indicate bRG cell soma, and green and red arrowheads indicate daughter cells.
Data are presented as mean values ± SD. Scale bar, 20 μm. All live imaging montages are in h and min. $^{**}p < 0.01$; $^{***}p < 0.001$; $^{****}p < 0.0001$; ns: non-significant by two-tailed unpaired t tests.

evolution and a process likely to be altered in several cortical malformations.

RESOURCE AVAILABILITY

Lead contact

Requests for further information and resources should be directed to and will be fulfilled by the lead contact, Alexandre D. Baffet (alexandre.baffet@curie.fr).

Materials availability

All reagents generated in this study are available from the lead contact with a completed materials transfer agreement.

Data and code availability

The sequencing data discussed in this publication have been deposited in NCBI's Gene Expression Omnibus and are accessible through GEO Series accession number GSE314657 (https://www.ncbi.nlm.nih.gov/geo/query/acc.cgi?acc=GSE314657). Any additional information required to reanalyze the data reported in this work is available from the lead contact upon request.

ACKNOWLEDGMENTS

R.W. was funded by a French Ministry of Research PhD fellowship and by a Fondation pour la Recherche Medicale (FRM) 4th-year fellowship. This work was funded by the ANR (ANR-20-CE16-0004-01) and by the Bettencourt Schueller Foundation Impulscience grant.

AUTHOR CONTRIBUTIONS

R.W., C.B., P.L., L.C., A.D.C., C.C., A.A., B.B., A.R., and F.B. performed experiments. R.W., C.B., P.L., and L.C. analyzed the data. M.C. and A.-S.M. developed tools for image analysis. X.W., J.-B.M., A.R., K.F.-N., and J.L. provided experimental models. A.B. acquired funding and supervised the project. R.W. and A.D.B. designed the project and wrote the manuscript.

DECLARATION OF INTERESTS

The authors declare no competing interests.

STAR★METHODS

Detailed methods are provided in the online version of this paper and include the following:

SUPPLEMENTAL INFORMATION

Supplemental information can be found online at https://doi.org/10.1016/j.neuron.2026.02.002.

Received: January 28, 2025
Revised: October 15, 2025
Accepted: February 3, 2026

REFERENCES

1. Herculano-Houzel, S. (2012). The remarkable, yet not extraordinary, human brain as a scaled-up primate brain and its associated cost. Proc. Natl. Acad. Sci. USA *109*, 10661–10668. https://doi.org/10.1073/pnas.1201895109.
2. Fernández, V., and Borrell, V. (2023). Developmental mechanisms of gyrification. Curr. Opin. Neurobiol. *80*, 102711. https://doi.org/10.1016/j.conb.2023.102711.
3. Allen, D.E., Donohue, K.C., Cadwell, C.R., Shin, D., Keefe, M.G., Sohal, V.S., and Nowakowski, T.J. (2022). Fate mapping of neural stem cell niches reveals distinct origins of human cortical astrocytes. Science *376*, 1441–1446. https://doi.org/10.1126/science.abm5224.
4. Delgado, R.N., Allen, D.E., Keefe, M.G., Mancia Leon, W.R., Ziffra, R.S., Crouch, E.E., Alvarez-Buylla, A., and Nowakowski, T.J. (2022). Individual human cortical progenitors can produce excitatory and inhibitory neurons. Nature *601*, 397–403. https://doi.org/10.1038/s41586-021-04230-7.
5. Del-Valle-Anton, L., Amin, S., Cimino, D., Neuhaus, F., Dvoretskova, E., Fernández, V., Babal, Y.K., Garcia-Frigola, C., Prieto-Colomina, A., Murcia-Ramón, R., et al. (2024). Multiple parallel cell lineages in the developing mammalian cerebral cortex. Sci. Adv. *10*, eadn9998. https://doi.org/10.1126/sciadv.adn9998.
6. He, Z., Dony, L., Fleck, J.S., Szałata, A., Li, K.X., Slišković, I., Lin, H.-C., Santel, M., Atamian, A., Quadrato, G., et al. (2024). An integrated transcriptomic cell atlas of human neural organoids. Nature *635*, 690–698. https://doi.org/10.1038/s41586-024-08172-8.
7. Li, Y., Li, Z., Wang, C., Yang, M., He, Z., Wang, F., Zhang, Y., Li, R., Gong, Y., Wang, B., et al. (2023). Spatiotemporal transcriptome atlas reveals the regional specification of the developing human brain. Cell *186*, 5892–5909. https://doi.org/10.1016/j.cell.2023.11.016.
8. Liu, D.D., He, J.Q., Sinha, R., Eastman, A.E., Toland, A.M., Morri, M., Neff, N.F., Vogel, H., Uchida, N., and Weissman, I.L. (2023). Purification and characterization of human neural stem and progenitor cells. Cell *186*, 1179–1194. https://doi.org/10.1016/j.cell.2023.02.017.
9. Uzquiano, A., Kedaigle, A.J., Pigoni, M., Paulsen, B., Adiconis, X., Kim, K., Faits, T., Nagaraja, S., Antón-Bolaños, N., Gerhardinger, C., et al. (2022). Proper acquisition of cell class identity in organoids allows definition of fate specification programs of the human cerebral cortex. Cell *185*, 3770–3788. https://doi.org/10.1016/j.cell.2022.09.010.
10. Fernández, V., Llinares-Benadero, C., and Borrell, V. (2016). Cerebral cortex expansion and folding: what have we learned? EMBO J. *35*, 1021–1044. https://doi.org/10.15252/embj.201593701.
11. Malatesta, P., Hartfuss, E., and Götz, M. (2000). Isolation of radial glial cells by fluorescent-activated cell sorting reveals a neuronal lineage. Development *127*, 5253–5263. https://doi.org/10.1242/dev.127.24.5253.
12. Noctor, S.C., Flint, A.C., Weissman, T.A., Dammerman, R.S., and Kriegstein, A.R. (2001). Neurons derived from radial glial cells establish

radial units in neocortex. Nature *409*, 714–720. https://doi.org/10.1038/35055553.

13. Nowakowski, T.J., Pollen, A.A., Sandoval-Espinosa, C., and Kriegstein, A.R. (2016). Transformation of the Radial Glia Scaffold Demarcates Two Stages of Human Cerebral Cortex Development. Neuron *91*, 1219–1227. https://doi.org/10.1016/j.neuron.2016.09.005.

14. Fietz, S.A., Kelava, I., Vogt, J., Wilsch-Bräuninger, M., Stenzel, D., Fish, J.L., Corbeil, D., Riehn, A., Distler, W., Nitsch, R., et al. (2010). OSVZ progenitors of human and ferret neocortex are epithelial-like and expand by integrin signaling. Nat. Neurosci. *13*, 690–699. https://doi.org/10.1038/nn.2553.

15. Hansen, D.V., Lui, J.H., Parker, P.R.L., and Kriegstein, A.R. (2010). Neurogenic radial glia in the outer subventricular zone of human neocortex. Nature *464*, 554–561. https://doi.org/10.1038/nature08845.

16. Reillo, I., De Juan Romero, C., García-Cabezas, M.Á., and Borrell, V. (2011). A Role for Intermediate Radial Glia in the Tangential Expansion of the Mammalian Cerebral Cortex. Cereb. Cortex *21*, 1674–1694. https://doi.org/10.1093/cercor/bhq238.

17. Sauerland, C., Menzies, B.R., Glatzle, M., Seeger, J., Renfree, M.B., and Fietz, S.A. (2018). The Basal Radial Glia Occurs in Marsupials and Underlies the Evolution of an Expanded Neocortex in Therian Mammals. Cereb. Cortex *28*, 145–157. https://doi.org/10.1093/cercor/bhw360.

18. Matsumoto, N., Tanaka, S., Horiike, T., Shinmyo, Y., and Kawasaki, H. (2020). A discrete subtype of neural progenitor crucial for cortical folding in the gyrencephalic mammalian brain. eLife *9*, e54873. https://doi.org/10.7554/eLife.54873.

19. Ostrem, B.E.L., Lui, J.H., Gertz, C.C., and Kriegstein, A.R. (2014). Control of Outer Radial Glial Stem Cell Mitosis in the Human Brain. Cell Rep. *8*, 656–664. https://doi.org/10.1016/j.celrep.2014.06.058.

20. Martínez-Martínez, M.Á., De Juan Romero, C., Fernández, V., Cárdenas, A., Götz, M., and Borrell, V. (2016). A restricted period for formation of outer subventricular zone defined by Cdh1 and Trnp1 levels. Nat. Commun. *7*, 11812. https://doi.org/10.1038/ncomms11812.

21. Liu, H., and Zhang, S.-C. (2011). Specification of neuronal and glial subtypes from human pluripotent stem cells. Cell. Mol. Life Sci. *68*, 3995–4008. https://doi.org/10.1007/s00018-011-0770-y.

22. Coquand, L., Brunet Avalos, C., Macé, A.-S., Farcy, S., Di Cicco, A., Lampic, M., Wimmer, R., Bessières, B., Attie-Bitach, T., Fraisier, V., et al. (2024). A cell fate decision map reveals abundant direct neurogenesis bypassing intermediate progenitors in the human developing neocortex. Nat. Cell Biol. *26*, 698–709. https://doi.org/10.1038/s41556-024-01393-z.

23. Lindenhofer, D., Haendeler, S., Esk, C., Littleboy, J.B., Brunet Avalos, C., Naas, J., Pflug, F.G., Van De Ven, E.G.P., Reumann, D., Baffet, A.D., et al. (2024). Cerebral organoids display dynamic clonal growth and tunable tissue replenishment. Nat. Cell Biol. *26*, 710–718. https://doi.org/10.1038/s41556-024-01412-z.

24. Andrews, M.G., Siebert, C., Wang, L., White, M.L., Ross, J., Morales, R., Donnay, M., Bamfonga, G., Mukhtar, T., McKinney, A.A., et al. (2023). LIF signaling regulates outer radial glial to interneuron fate during human cortical development. Cell Stem Cell *30*, 1382–1391. https://doi.org/10.1016/j.stem.2023.08.009.

25. Qian, X., Su, Y., Adam, C.D., Deutschmann, A.U., Pather, S.R., Goldberg, E.M., Su, K., Li, S., Lu, L., Jacob, F., et al. (2020). Sliced Human Cortical Organoids for Modeling Distinct Cortical Layer Formation. Cell Stem Cell *26*, 766–781. https://doi.org/10.1016/j.stem.2020.02.002.

26. Walsh, R.M., Luongo, R., Giacomelli, E., Ciceri, G., Rittenhouse, C., Verrillo, A., Galimberti, M., Bocchi, V.D., Wu, Y., Xu, N., et al. (2024). Generation of human cerebral organoids with a structured outer subventricular zone. Cell Rep. *43*, 114031. https://doi.org/10.1016/j.celrep.2024.114031.

27. Florio, M., Albert, M., Taverna, E., Namba, T., Brandl, H., Lewitus, E., Haffner, C., Sykes, A., Wong, F.K., Peters, J., et al. (2015). Human-specific gene *ARHGAP11B* promotes basal progenitor amplification and neocortex expansion. Science *347*, 1465–1470. https://doi.org/10.1126/science.aaa1975.

28. Ju, X.-C., Hou, Q.-Q., Sheng, A.-L., Wu, K.-Y., Zhou, Y., Jin, Y., Wen, T., Yang, Z., Wang, X., and Luo, Z.-G. (2016). The hominoid-specific gene TBC1D3 promotes generation of basal neural progenitors and induces cortical folding in mice. eLife *5*, e18197. https://doi.org/10.7554/eLife.18197.

29. Liu, J., Liu, W., Yang, L., Wu, Q., Zhang, H., Fang, A., Li, L., Xu, X., Sun, L., Zhang, J., et al. (2017). The Primate-Specific Gene TMEM14B Marks Outer Radial Glia Cells and Promotes Cortical Expansion and Folding. Cell Stem Cell *21*, 635–649. https://doi.org/10.1016/j.stem.2017.08.013.

30. Fiddes, I.T., Lodewijk, G.A., Mooring, M., Bosworth, C.M., Ewing, A.D., Mantalas, G.L., Novak, A.M., Van Den Bout, A., Bishara, A., Rosenkrantz, J.L., et al. (2018). Human-Specific NOTCH2NL Genes Affect Notch Signaling and Cortical Neurogenesis. Cell *173*, 1356–1369. https://doi.org/10.1016/j.cell.2018.03.051.

31. Suzuki, I.K., Gacquer, D., Van Heurck, R., Kumar, D., Wojno, M., Bilheu, A., Herpoel, A., Lambert, N., Cheron, J., Polleux, F., et al. (2018). Human-Specific NOTCH2NL Genes Expand Cortical Neurogenesis through Delta/Notch Regulation. Cell *173*, 1370–1384. https://doi.org/10.1016/j.cell.2018.03.067.

32. Fischer, J., Fernández Ortuño, E., Marsoner, F., Artioli, A., Peters, J., Namba, T., Eugster Oegema, C., Huttner, W.B., Ladewig, J., and Heide, M. (2022). Human-specific *ARHGAP11B* ensures human-like basal progenitor levels in hominid cerebral organoids. EMBO Rep. *23*, e54728. https://doi.org/10.15252/embr.202254728.

33. Pinson, A., Xing, L., Namba, T., Kalebic, N., Peters, J., Oegema, C.E., Traikov, S., Reppe, K., Riesenberg, S., Maricic, T., et al. (2022). Human TKTL1 implies greater neurogenesis in frontal neocortex of modern humans than Neanderthals. Science *377*, eabl6422. https://doi.org/10.1126/science.abl6422.

34. Xing, L., Gkini, V., Nieminen, A.I., Zhou, H.-C., Aquilino, M., Naumann, R., Reppe, K., Tanaka, K., Carmeliet, P., Heikinheimo, O., et al. (2024). Functional synergy of a human-specific and an ape-specific metabolic regulator in human neocortex development. Nat. Commun. *15*, 3468. https://doi.org/10.1038/s41467-024-47437-8.

35. Betizeau, M., Cortay, V., Patti, D., Pfister, S., Gautier, E., Bellemin-Ménard, A., Afanassieff, M., Huissoud, C., Douglas, R.J., Kennedy, H., et al. (2013). Precursor Diversity and Complexity of Lineage Relationships in the Outer Subventricular Zone of the Primate. Neuron *80*, 442–457. https://doi.org/10.1016/j.neuron.2013.09.032.

36. Kalebic, N., Gilardi, C., Stepien, B., Wilsch-Bräuninger, M., Long, K.R., Namba, T., Florio, M., Langen, B., Lombardot, B., Shevchenko, A., et al. (2019). Neocortical Expansion Due to Increased Proliferation of Basal Progenitors Is Linked to Changes in Their Morphology. Cell Stem Cell *24*, 535–550. https://doi.org/10.1016/j.stem.2019.02.017.

37. Huang, W., Bhaduri, A., Velmeshev, D., Wang, S., Wang, L., Rottkamp, C.A., Alvarez-Buylla, A., Rowitch, D.H., and Kriegstein, A.R. (2020). Origins and Proliferative States of Human Oligodendrocyte Precursor Cells. Cell *182*, 594–608. https://doi.org/10.1016/j.cell.2020.06.027.

38. Andrews, M.G., Subramanian, L., and Kriegstein, A.R. (2020). mTOR signaling regulates the morphology and migration of outer radial glia in developing human cortex. eLife *9*, e58737. https://doi.org/10.7554/eLife.58737.

39. Qian, X., Nguyen, H.N., Song, M.M., Hadiono, C., Ogden, S.C., Hammack, C., Yao, B., Hamersky, G.R., Jacob, F., Zhong, C., et al. (2016). Brain-Region-Specific Organoids Using Mini-bioreactors for Modeling ZIKV Exposure. Cell *165*, 1238–1254. https://doi.org/10.1016/j.cell.2016.04.032.

40. Sloan, S.A., Andersen, J., Paşca, A.M., Birey, F., and Paşca, S.P. (2018). Generation and assembly of human brain region-specific three-dimensional cultures. Nat. Protoc. *13*, 2062–2085. https://doi.org/10.1038/s41596-018-0032-7.

41. Wimmer, R., and Baffet, A.D. (2023). The microtubule cytoskeleton of radial glial progenitor cells. Curr. Opin. Neurobiol. *80*, 102709. https://doi.org/10.1016/j.conb.2023.102709.

42. Spear, P.C., and Erickson, C.A. (2012). Apical movement during interkinetic nuclear migration is a two-step process. Dev. Biol. *370*, 33–41. https://doi.org/10.1016/j.ydbio.2012.06.031.

43. Pilaz, L.-J., Patti, D., Marcy, G., Ollier, E., Pfister, S., Douglas, R.J., Betizeau, M., Gautier, E., Cortay, V., Doerflinger, N., et al. (2009). Forced G1-phase reduction alters mode of division, neuron number, and laminar phenotype in the cerebral cortex. Proc. Natl. Acad. Sci. USA *106*, 21924–21929. https://doi.org/10.1073/pnas.0909894106.

44. Sakaue-Sawano, A., Kurokawa, H., Morimura, T., Hanyu, A., Hama, H., Osawa, H., Kashiwagi, S., Fukami, K., Miyata, T., Miyoshi, H., et al. (2008). Visualizing Spatiotemporal Dynamics of Multicellular Cell-Cycle Progression. Cell *132*, 487–498. https://doi.org/10.1016/j.cell.2007.12.033.

45. Koh, S.-B., Mascalchi, P., Rodriguez, E., Lin, Y., Jodrell, D.I., Richards, F.M., and Lyons, S.K. (2017). A quantitative FastFUCCI assay defines cell cycle dynamics at a single-cell level. J. Cell Sci. *130*, 512–520. https://doi.org/10.1242/jcs.195164.

46. Reiner, O., Carrozzo, R., Shen, Y., Wehnert, M., Faustinella, F., Dobyns, W.B., Caskey, C.T., and Ledbetter, D.H. (1993). Isolation of a Miller–Dicker lissencephaly gene containing G protein β-subunit-like repeats. Nature *364*, 717–721. https://doi.org/10.1038/364717a0.

47. Iefremova, V., Manikakis, G., Krefft, O., Jabali, A., Weynans, K., Wilkens, R., Marsoner, F., Brändl, B., Müller, F.-J., Koch, P., et al. (2017). An Organoid-Based Model of Cortical Development Identifies Non-Cell-Autonomous Defects in Wnt Signaling Contributing to Miller-Dieker Syndrome. Cell Rep. *19*, 50–59. https://doi.org/10.1016/j.celrep.2017.03.047.

48. Zillich, L., Gasparotto, M., Rossetti, A.C., Fechtner, O., Maillard, C., Hoffrichter, A., Zillich, E., Jabali, A., Marsoner, F., Artioli, A., et al. Capturing the biology of disease severity in an organoid model of LIS1-lissencephaly. Preprint at bioRxiv. https://doi.org/10.1101/2022.12.19.520907

49. Hu, D.J.-K., Baffet, A.D., Nayak, T., Akhmanova, A., Doye, V., and Vallee, R.B. (2013). Dynein Recruitment to Nuclear Pores Activates Apical Nuclear Migration and Mitotic Entry in Brain Progenitor Cells. Cell *154*, 1300–1313. https://doi.org/10.1016/j.cell.2013.08.024.

50. Luxton, G.W.G., Gomes, E.R., Folker, E.S., Vintinner, E., and Gundersen, G.G. (2010). Linear Arrays of Nuclear Envelope Proteins Harness Retrograde Actin Flow for Nuclear Movement. Science *329*, 956–959. https://doi.org/10.1126/science.1189072.

51. Splinter, D., Tanenbaum, M.E., Lindqvist, A., Jaarsma, D., Flotho, A., Yu, K.L., Grigoriev, I., Engelsma, D., Haasdijk, E.D., Keijzer, N., et al. (2010). Bicaudal D2, Dynein, and Kinesin-1 Associate with Nuclear Pore Complexes and Regulate Centrosome and Nuclear Positioning during Mitotic Entry. PLoS Biol. *8*, e1000350. https://doi.org/10.1371/journal.pbio.1000350.

52. Taubenberger, A.V., Baum, B., and Matthews, H.K. (2020). The Mechanics of Mitotic Cell Rounding. Front. Cell Dev. Biol. *8*, 687. https://doi.org/10.3389/fcell.2020.00687.

53. Kunda, P., Pelling, A.E., Liu, T., and Baum, B. (2008). Moesin Controls Cortical Rigidity, Cell Rounding, and Spindle Morphogenesis during Mitosis. Curr. Biol. *18*, 91–101. https://doi.org/10.1016/j.cub.2007.12.051.

54. Ramanathan, S.P., Helenius, J., Stewart, M.P., Cattin, C.J., Hyman, A.A., and Muller, D.J. (2015). Cdk1-dependent mitotic enrichment of cortical myosin II promotes cell rounding against confinement. Nat. Cell Biol. *17*, 148–159. https://doi.org/10.1038/ncb3098.

55. Toyoda, Y., Cattin, C.J., Stewart, M.P., Poser, I., Theis, M., Kurzchalia, T.V., Buchholz, F., Hyman, A.A., and Müller, D.J. (2017). Genome-scale single-cell mechanical phenotyping reveals disease-related genes involved in mitotic rounding. Nat. Commun. *8*, 1266. https://doi.org/10.1038/s41467-017-01147-6.

56. Duarte, S., Viedma-Poyatos, Á., Navarro-Carrasco, E., Martínez, A.E., Pajares, M.A., and Pérez-Sala, D. (2019). Vimentin filaments interact with the actin cortex in mitosis allowing normal cell division. Nat. Commun. *10*, 4200. https://doi.org/10.1038/s41467-019-12029-4.

57. Serres, M.P., Samwer, M., Truong Quang, B.A., Lavoie, G., Perera, U., Görlich, D., Charras, G., Petronczki, M., Roux, P.P., and Paluch, E.K. (2020). F-Actin Interactome Reveals Vimentin as a Key Regulator of Actin Organization and Cell Mechanics in Mitosis. Dev. Cell *52*, 210–222. https://doi.org/10.1016/j.devcel.2019.12.011.

58. Nyga, A., Plak, K., Kräter, M., Urbanska, M., Kim, K., Guck, J., and Baum, B. (2023). Dynamics of cell rounding during detachment. iScience *26*, 106696. https://doi.org/10.1016/j.isci.2023.106696.

59. Raaijmakers, J.A., Tanenbaum, M.E., and Medema, R.H. (2013). Systematic dissection of dynein regulators in mitosis. J. Cell Biol. *201*, 201–215. https://doi.org/10.1083/jcb.201208098.

60. Bhaduri, A., Di Lullo, E., Jung, D., Müller, S., Crouch, E.E., Espinosa, C.S., Ozawa, T., Alvarado, B., Spatazza, J., Cadwell, C.R., et al. (2020). Outer Radial Glia-like Cancer Stem Cells Contribute to Heterogeneity of Glioblastoma. Cell Stem Cell *26*, 48–63. https://doi.org/10.1016/j.stem.2019.11.015.

61. Wang, R., Sharma, R., Shen, X., Laughney, A.M., Funato, K., Clark, P.J., Shpokayte, M., Morgenstern, P., Navare, M., Xu, Y., et al. (2020). Adult Human Glioblastomas Harbor Radial Glia-like Cells. Stem Cell Rep. *14*, 338–350. https://doi.org/10.1016/j.stemcr.2020.01.007.

62. Eisenbarth, D., and Wang, Y.A. (2023). Glioblastoma heterogeneity at single cell resolution. Oncogene *42*, 2155–2165. https://doi.org/10.1038/s41388-023-02738-y.

63. Xie, Y., Bergström, T., Jiang, Y., Johansson, P., Marinescu, V.D., Lindberg, N., Segerman, A., Wicher, G., Niklasson, M., Baskaran, S., et al. (2015). The Human Glioblastoma Cell Culture Resource: Validated Cell Models Representing All Molecular Subtypes. EBiomedicine *2*, 1351–1363. https://doi.org/10.1016/j.ebiom.2015.08.026.

64. Baffet, A.D., Hu, D.J., and Vallee, R.B. (2015). Cdk1 Activates Pre-mitotic Nuclear Envelope Dynein Recruitment and Apical Nuclear Migration in Neural Stem Cells. Dev. Cell *33*, 703–716. https://doi.org/10.1016/j.devcel.2015.04.022.

65. Tsai, J.-W., Bremner, K.H., and Vallee, R.B. (2007). Dual subcellular roles for LIS1 and dynein in radial neuronal migration in live brain tissue. Nat. Neurosci. *10*, 970–979. https://doi.org/10.1038/nn1934.

66. Gonçalves, J.C., Quintremil, S., Yi, J., and Vallee, R.B. (2020). Nesprin-2 Recruitment of BicD2 to the Nuclear Envelope Controls Dynein/Kinesin-Mediated Neuronal Migration In Vivo. Curr. Biol. *30*, 3116–3129. https://doi.org/10.1016/j.cub.2020.05.091.

67. Qian, X., Coleman, K., Jiang, S., Kriz, A.J., Marciano, J.H., Luo, C., Cai, C., Manam, M.D., Caglayan, E., Otani, A., et al. (2024). Spatial Single-cell Analysis Decodes Cortical Layer and Area Specification. Preprint at bioRxiv. https://doi.org/10.1101/2024.06.05.597673.

68. Wang, L., Wang, C., Moriano, J.A., Chen, S., Zuo, G., Cebrián-Silla, A., Zhang, S., Mukhtar, T., Wang, S., Song, M., et al. (2024). Molecular and cellular dynamics of the developing human neocortex at single-cell resolution. Preprint at bioRxiv. https://doi.org/10.1101/2024.01.16.575956.

69. Kyrousi, C., O'Neill, A.C., Brazovskaja, A., He, Z., Kielkowski, P., Coquand, L., Di Giaimo, R., D' Andrea, P., Belka, A., Forero Echeverry, A., et al. (2021). Extracellular LGALS3BP regulates neural progenitor

position and relates to human cortical complexity. Nat. Commun. *12*, 6298. https://doi.org/10.1038/s41467-021-26447-w.

70. Gaignerie, A., Lefort, N., Rousselle, M., Forest-Choquet, V., Flippe, L., Francois-Campion, V., Girardeau, A., Caillaud, A., Chariau, C., Francheteau, Q., et al. (2018). Urine-derived cells provide a readily accessible cell type for feeder-free mRNA reprogramming. Sci. Rep. *8*, 14363. https://doi.org/10.1038/s41598-018-32645-2.

71. Bhaduri, A., Sandoval-Espinosa, C., Otero-Garcia, M., Oh, I., Yin, R., Eze, U.C., Nowakowski, T.J., and Kriegstein, A.R. (2021). An atlas of cortical arealization identifies dynamic molecular signatures. Nature *598*, 200–204. https://doi.org/10.1038/s41586-021-03910-8.

72. Speir, M.L., Bhaduri, A., Markov, N.S., Moreno, P., Nowakowski, T.J., Papatheodorou, I., Pollen, A.A., Raney, B.J., Seninge, L., Kent, W.J., et al. (2021). UCSC Cell Browser: visualize your single-cell data. Bioinformatics *37*, 4578–4580. https://doi.org/10.1093/bioinformatics/btab503.

Please cite this article in press as: Wimmer et al., Two translocation mechanisms drive neural stem cell dissemination into the human fetal cortex, Neuron (2026), https://doi.org/10.1016/j.neuron.2026.02.002

STAR★METHODS

KEY RESOURCES TABLE

REAGENT or RESOURCE	SOURCE	IDENTIFIER
Antibodies		
Mouse Anti-SOX2	Abcam	Cat# ab79351; RRID:AB_10710406
Sheep Anti-EOMES	R&D Systems	Cat# AF6166; RRID:AB_10569705
Rabbit Anti-NeuN	Abcam	Cat# ab177487; RRID:AB_2532109
Chicken Anti-GFP	Abcam	Cat# ab13970; RRID:AB_300798
Mouse Anti-Vimentin Phospho (Ser55)	Abcam	Cat# ab22651, RRID:AB_447222
Rabbit Anti-NeuroD2	Abcam	Cat# ab104430, RRID:AB_10975628
Rabbit Anti-HOPX	Proteintech	Cat# 11419-1-AP, RRID:AB_10693525
Rabbit Anti-Nesprin 2	Abcam	Cat# ab204308, RRID:AB_3718095
Rabbit Anti-Histone H3 (phospho S10)	Abcam	Cat# ab47297, RRID:AB_880448
Mouse Anti-gamma-Tubulin	Sigma-Aldrich	Cat# T5326, RRID:AB_532292
Rabbit Anti-Phospho-Ezrin (Thr567)/ Radixin (Thr564)/Moesin (Thr558)	Cell Signaling Technologies	Cat# 3141S, RRID:AB_3719569)
Mouse Anti-LIFR	Abcam	Cat# ab89792, RRID:AB_2136107
Rabbit Anti-PTPRZ1	Atlas Antibodies	Cat# HPA015103, RRID:AB_1855946
Rabbit Anti-Myosin Light Chain (Phospho Ser19)	Cell Signaling Technologies	Cat# 3671, RRID:AB_330248
Bacterial and virus strains		
MSCV-IRES-GFP	Unpublished	Addgene, RRID:Addgene_20672
pBOB-EF1-FastFUCCI-Puro	Koh et al.[45]	Addgene, RRID:Addgene_86849
pLV[Exp]-CMV>mCherry(ns):3xGGGGS	Vectorbuilder	VB250528-1313huf
pCAG-VSVG	Unpublished	Addgene, RRID:Addgene_35616
Human EZR shRNA	Origene	TF308420
Human DYNC1H1 shRNA	Origene	TL313335
Human RDX shRNA	Origene	TL309884
Human MSN shRNA	Origene	TL311375
Human VIM shRNA	Origene	TL308419
Human PAFAH1B1 (LIS1) shRNA	Origene	TL310628
Dominant (-) KASH	This paper	N/A
Biological samples		
Human Fetal Brain tissue samples	Dr. Fabien Guimiot (Hopital Robert Debré) & Dr Bettina Bessière (Hopital Necker) Agence Française de Biomédecine	Agence Française de Biomédecine (PFS17-003)
Chemicals, peptides, and recombinant proteins		
(−)-Blebbistatin	Sigma-Aldrich	B0560; CAS:856925-71-8
Nocodazol	Merck	M1404; CAS:31430-18-9
RO-3306	Merck	SML0569; CAS: 872573-93-8
Accutase	StemCell Technologies	#07920; CAS: N/A
Deposited data		
RNA-seq data (https://www.ncbi.nlm.nih.gov/geo/query/acc.cgi?acc=GSE314657)	NCBI Gene Expression Omnibus	GSE314657
Experimental models: Cell lines		
HEK-Phoenix-GP Human Embryonic Kidney Cell line	ATCC	CRL-3215
HEK T293 Human Embryonic Kidney Cell line	ATCC	CRL-1573
U3008 Human Glioblastoma Cell Line	HGCC Uppsala University	CVCL_IR59

(*Continued on next page*)

Continued

REAGENT or RESOURCE	SOURCE	IDENTIFIER
U3009 Human Glioblastoma Cell Line	HGCC Uppsala University	CVCL_IR60
U3017 Human Glioblastoma Cell Line	HGCC Uppsala University	CVCL_IR63
U3021 Human Glioblastoma Cell Line	HGCC Uppsala University	CVCL_IR66
U3031 Human Glioblastoma Cell Line	HGCC Uppsala University	CVCL_IR71
U3039 Human Glioblastoma Cell Line	HGCC Uppsala University	CVCL_IR76
U3047 Human Glioblastoma Cell Line	HGCC Uppsala University	CVCL_IR79
U3065 Human Glioblastoma Cell Line	HGCC Uppsala University	CVCL_IR87
U3088 Human Glioblastoma Cell Line	HGCC Uppsala University	CVCL_IR97
U3123 Human Glioblastoma Cell Line	HGCC Uppsala University	CVCL_IS03
HMGU#1 (ISFi001-A) iPS cell line	Helmholtz Munich	CVCL_YT30
f71.002 wild type iPS cell line	Plateforme iPSC Nantes	N f71.002
Software and algorithms		
ImageJ	N/A	https://imagej.nih.gov/ij/
GraphPad Prism 10.6.0	N/A	https://www.graphpad.com
R (v4.5.x) with Bioconductor (v3.21)	N/A	https://www.r-project.org/

EXPERIMENTAL MODEL AND STUDY PARTICIPANT DETAILS

Human fetal tissue

Human fetal tissue samples were collected with previous patient consent and in strict observance of legal and institutional ethical regulations. The protocol was approved by the French biomedical agency (Agence de la Biomédecine, approval number: PFS17-003). The fetal human neocortex tissue samples used in this study reported no health disorders, these tissues were derived from spontaneous miscarriages. The procedure is described in detail in the 'Infection of human fetal cortex and cortical organoids' section of the methods. No participant was compensated in this study. Fresh human fetal prefrontal cortex samples were obtained from autopsies conducted at Robert Debré Hospital and Necker-Enfants Malades Hospital in Paris. A sample of the pre-frontal cortex was excised from one hemisphere and transported on ice to the laboratory. For reasons of data-privacy protection, the sex of the human fetuses used to obtain neocortical tissue cannot be reported. This variable is not anticipated to affect the findings of this study.

Human induced pluripotent stem cell lines

The feeder-independent induced pluripotent stem (iPS) cell lines used for this study were obtained through collaborations with the laboratory of Silvia Cappello (Max Planck Institute of Psychiatry), Julia Ladewig (Hector Institute for Translational Brain Research) and Laurent David (University of Nantes). All experiments involving iPS cells were performed in accordance with the ethical standards of the institutional and/or national research committee. HMGU1 cells were reprogrammed from NuFF3-RQ human newborn foreskin feeder fibroblasts – male donor – (GSC-3404, Global Stel).[69] The f71.002 wild-type line – from a female donor[70] – was a kind gift from Laurent David (iPSC core facility from Nantes Université, supported by IBiSA and Biogenouest). No difference between male and female lines were observed. iPS cells were cultivated as colonies on vitronectin-coated B3 dishes, using StemFlex medium (Thermo Fisher Scientific). Colonies were cleaned every two days under a binocular stereo microscope (Lynx EVO, Vision Engineering), by manually removing differentiated cells with a needle. Two independent LIS1-mutated patient derived iPS cells were obtained from the laboratory of Julia Ladewig. Patient #1, LIS1-severe 1, 4-year-old female donor, c.1002+1G>T and patient #2 LIS1-severe 2, 18-year-old female donor, c.531G>C LIS1-mutation. Each patient specific mutation was confirmed through Sanger sequencing and quality control by the laboratory of origin.[48]

Glioblastoma cell lines

Patient-derived glioblastoma cells were acquired from the Human Glioblastoma Cell Culture resource (www.hgcc.se) at the Dept. of Immunology, Genetics and Pathology, Uppsala University, Uppsala, Sweden and are a part of collaboration through a Material Transfer Agreement between Institute Curie and Uppsala University.[63] U3008, U3009, U3017, U3021, U3031, U3039, U3047, U3065, U3088, U3123 cell lines from the HGCC biobank were cultured in cell culture plastic dishes coated with Matrigel in culture medium containing 50% DMEM-F12 and 50% Neurobasal Medium, penicillin/streptomycin 1U/mL, B27 (-vitamin A), EGF 10ng/ml and FGF 10ng/ml. At confluency for imaging or for maintenance, cells were detached using pre-warmed accutase and replated in Matrigel coated dishes. Treatment of these cells with nocodazole (1μM), blebbistatin (10μM) or infection with different viral particles and subsequent imaging was done as described for in vitro radial glial cells. For reasons of data-privacy protection, the sex of the glioblastoma cell lines cannot be reported. This variable is not anticipated to affect the findings of this study.

Sample size estimation

No statistical methods were used to predetermine sample size. Sample sizes were based on the availability of human samples and are consistent with those commonly used in comparable studies in the field. Experiments were performed on independent biological samples as indicated in the figure legends, and key findings were reproduced across multiple donors and/or independent experimental replicates to ensure robustness.

Allocation of samples to experimental groups

Samples were allocated to experimental groups based on experimental design and sample availability. Where applicable, samples from the same donor were split and processed in parallel across experimental conditions to minimize inter-individual variability. Allocation was not randomized, as samples were not drawn from a pre-defined cohort but obtained based on availability. No exclusion criteria were applied after sample allocation.

METHOD DETAILS

Virus production

We employed the HEK-Phoenix-GP cell line obtained from ATCC (CRL-3215), which stably expresses the packaging enzymes GAL and POL. Cells were seeded in 4×T300 flasks at a 1:20 dilution and cultured for three days in DMEM-GlutaMAX medium supplemented with 10% fetal bovine serum (FBS) (50 ml per flask) until they reached approximately 70% confluence. On the third day, the cells were transfected with an envelope VSVG plasmid and a transfer plasmid (either CAG-GFP or MSCV-IRES-GFP) using Lipofectamine 2000. For this, the plasmids were mixed in 14.4 ml of OptiMEM medium (24 μg of envelope plasmid and 66 μg of transfer plasmid). Concurrently, 450 μl of Lipofectamine 2000 was diluted in 14.4 ml of OptiMEM medium and allowed to incubate for 5 minutes at room temperature. The DNA mixture was then combined with the Lipofectamine solution and incubated for an additional 30 minutes at room temperature. Meanwhile, the medium in each T300 flask was replaced with 30 ml of DMEM-GlutaMAX (without FBS). Following the incubation, 3.6 ml of the DNA-Lipofectamine mixture was added to each flask, and the cells were incubated for 5 hours at 37°C. For lentiviral production, we used HEK T293 cells. Cells were plated in 3xT150 (dilution 1:20) and grown for 3 days to reach 70% confluency in DMEM-GlutaMAX medium, 10% foetal bovine serum (FBS) (30 ml per flask). On day 3, cells were transfected with PMD2G (an envelope expressing VSVG), PMAX2 (a second packaging vector) and the transfer plasmid. Subsequently, the retrovirus and lentivirus flasks were moved to an L3 laboratory where the medium was replaced with 30 ml of fresh DMEM-GlutaMAX containing 10% FBS. On the fifth day, the medium was harvested into 50 ml tubes, replaced with 30 ml of fresh medium, and stored at 4°C. On the sixth day, the medium was again collected, pooled with the day 5 samples, and centrifuged at 1,300 rpm for 5 minutes at 4°C to pellet cell debris. The supernatant was then filtered through a 0.22 μm filter unit and distributed into six Ultra-Clear tubes (Beckman Coulter, 344058). These tubes were ultracentrifuged at 31,000g for 90 minutes at 4°C. The supernatant was discarded, and the retrovirus-containing pellet was washed several times with PBS and transferred to a new Ultra-Clear tube. A final ultracentrifugation step was performed (31,000g for 90 minutes at 4°C), after which the supernatant was carefully removed, and the retrovirus pellet was resuspended in 1 ml of DMEM-F12 medium. The suspension was aliquoted (50 to 100 μl per aliquot) and stored at -80°C. The viral titer of the preparation was assessed by infecting standard HEK cells at various dilutions, and the proportion of GFP-positive cells was determined using fluorescence-activated cell sorting (FACS).

Generation of cortical organoids

Cortical organoids were generated from human induced pluripotent stem (iPS) cells following an adapted protocol from previously published.[39,40] Day 0 to Day 4: iPS cell colonies were detached using pre-warmed collagenase (1 mg/ml) for 45 minutes at 37°C. The floating colonies were transferred using a cut pipette tip into a 15 ml tube and washed with Medium 1 (DMEM-F12 without phenol red, 20% KnockOut Serum Replacement (KSR), 1× GlutaMAX, 1× MEM Non-Essential Amino Acids (MEM-NEAA), 1× 2-mercaptoethanol, penicillin/streptomycin, 2 μM Dorsomorphin, 2 μM A-83). The colonies were then transferred into ultra-low attachment plates with 3 ml of Medium 1 and cultured at 37°C in a 5% CO2 atmosphere. Day 5 to Day 6: Half of the Medium 1 was replaced daily with Medium 2 (DMEM-F12 without phenol red, 1× N2 supplement, 1× GlutaMAX, 1× MEM-NEAA, penicillin/streptomycin, 1 μM CHIR-99021, 1 μM SB-431542). Day 7 to Day 14: On Day 7, embryoid bodies (EBs) were embedded in Matrigel diluted in Medium 2 at a ratio of 2:1. The Matrigel-EB mixture was spread into regular 6-well plates and incubated at 37°C for 30 minutes to solidify (10–20 EBs per well). Medium 2 was gently added to the well without disturbing the Matrigel patch. On Day 14, the Matrigel-EB mixture was mechanically dissociated using a 5 ml pipette and transferred into a 15 ml tube for gentle washing. Organoids were then suspended in Medium 3 (DMEM-F12 without phenol red, 1× N2 supplement, 1× B27 supplement (with vitamin A), 1×GlutaMAX, 1×MEM-NEAA, 1× 2-mercaptoethanol, penicillin/streptomycin, 2.5 μg/ml insulin) and cultured in ultra-low Attachment 6-well plates under agitation at 100 rpm using a Digital Orbital Shaker (DOS-10M from ELMI). Day 35 to Day 84: Starting from Day 35, Medium 3 was supplemented every two days with diluted Matrigel (1:100) to support the growth and development of the cortical organoids.

Culture and infection of human fetal tissue

Human fetal tissue was subdivided into smaller pieces and embedded in 4% low-gelling agarose (Sigma), which was dissolved in DMEM-F12. Cortical organoids (8–12 weeks) were embedded in 3% low-gelling agarose. Both types of tissue were sectioned

Please cite this article in press as: Wimmer et al., Two translocation mechanisms drive neural stem cell dissemination into the human fetal cortex, Neuron (2026), https://doi.org/10.1016/j.neuron.2026.02.002

into 300-μm-thick slices using a Leica VT1200S vibratome in ice-cold DMEM-F12. The slices were infected with a GFP-coding retrovirus diluted in DMEM-F12. After a 2-hour incubation period, the slices were washed three times with DMEM-F12 and cultured on Millicell cell culture inserts (Merck) in cortical culture medium (DMEM-F12 supplemented with B27, N2, 10 ng/ml fibroblast growth factor (FGF), 10 ng/ml epidermal growth factor (EGF), 5% foetal bovine serum, and 5% normal horse serum).

Live imaging of fetal brain tissue and cortical organoids slices

Fetal tissue (96 hours post-infection) and organoid slices (48 hours post-infection) were transferred to a 35 mm FluoroDish (WPI) containing 1 ml of cortical culture medium. 48 to 96-hour live imaging was performed using a spinning disk-wide microscope equipped with a Yokogawa CSU-W1 scanner unit to enhance the field of view and resolution. The microscope was equipped with a high working distance (WD 6.9–8.2 mm) ×20 Plan Fluor ELWD NA 0.45 dry objective (Nikon) and a Prime95B SCMOS camera. Z-stacks ranging from 100 to 110 μm were captured at 5 μm intervals, and maximum projections were generated. Videos were assembled and processed using Fiji ImageJ, with maximum projections, background subtraction, median filtering, stack registration, and rotation adjustments applied.

Live and fixed correlative microscopy analysis

Live–fixed correlative microscopy was carried out as previously described using the published *LiveFixedCorrelative* ImageJ/MATLAB macro.[22] This method enables automated contour detection, sample matching based on area and morphology, and alignment through rotation or flipping when required, allowing precise localization of live-imaged cells within the corresponding immunostained sections. Newly acquired data were analyzed together with reanalyzed datasets from the original publication.

Electroporation and 21-day imaging of human fetal cortex slices

Tissue samples were embedded in 4% low-gelling agarose prepared in artificial cerebrospinal fluid (ACSF). Fast Green–labeled DNA (DN-KASH, MSNshRNA and MSCV-GFP) was injected through the agarose at the ventricular surface using a micro-needle. Electrodes were positioned on opposite sides of the agarose block, with the negative pole oriented toward the ventricular surface and the positive pole facing the cortical plate. Electroporation was performed by delivering five pulses of 50 V for 50 ms each. Following electroporation, tissues were sectioned at 300 μm in cold ACSF using a vibratome and cultured on Millicell inserts for up to three weeks. Slices were maintained in media with half of the medium replaced daily at 37 °C and 5% CO_2 to preserve physiological conditions. Slices were imaged every 7 days using a Nikon spinning-disk microscope with a 25 mm field-of-view (2048 × 2048 pixels, 2K resolution) and a dry 10× objective (NA 0.45, WD 4 0.17). Tissues with selected constructs were visualized in the GFP channel at 15% laser power and 500ms exposure time, while the tissue architecture was acquired in brightfield at 10% laser power, 50ms exposure time. Mosaic reconstructions were generated in NIS-Elements software to stitch and overlay channels, enabling simultaneous visualization of transfected cells in the fetal brain tissue. During imaging, cultures were maintained on a Tokai heating stage at 37 °C and 5% CO_2 to preserve physiological conditions.

Immunostaining of fetal brain tissue and cortical organoids slices

Cortical organoid or fetal cortex tissue slices were fixed with 4% paraformaldehyde (PFA) for 20–30 min at room temperature or overnight at 4 °C, followed by 3–5 quick washes with PBS. Permeabilization and blocking were performed for 1 h at room temperature with agitation using PerBlocking Solution (0.25% Triton X-100, 5% normal donkey serum in PBS). Primary antibodies were diluted in Blocking Solution (0.01% Triton X-100, 5% normal donkey serum in PBS) (300 μL per well) and incubated overnight at 4 °C with agitation. Samples were washed with 0.1% PBST (0.1% Triton X-100 in PBS) using 3–5 quick washes followed by 3 × 20 min washes at room temperature. Secondary antibodies were prepared in Blocking Solution (0.1% Triton X-100, 5% normal donkey serum in PBS, 300 μL per well) and incubated overnight at 4 °C with light protection and agitation. Washes were repeated as above. Samples were mounted using Aqua Poly/Mount and allowed to polymerize overnight at room temperature. Imaging was performed after mounting.

Isolation and culture of human fetal radial glial cells

Fresh human fetal prefrontal cortex tissue was washed with culture medium (DMEM-F12, D-glucose 2.9 mg/mL, penicillin/streptomycin 5U/mL, amphotericin 250ng/mL) and replaced by culture medium supplemented with B27 (-vitamin A), FGF 20 ng/mL and EGF 20 ng/mL. The tissue was then disassociated by mechanical trituration with a pipette. The suspension was spun down at 1200rpm for 3mins and the pellet suspended into 1mL of supplemented culture media. After viability was checked (70%–90%), the cells were plated into 6 well plates coated with 0.1 mg/mL poly-D-lysine and 1.5% fibronectin, in 2mL of culture media at a density of 2.000.000 cells per well. The cells were incubated at 37°C, 5% C02. The culture medium was replaced the day after and every two days afterwards to remove floating cells and debris. 2–3 weeks later, depending on the tissue stage, radial glia cells were detached with pre-warmed accutase for 10mins at 37°C, 5% C02 and replated into novel pre-coated plates. Cells were checked for fate markers at each consecutive passage by fixing with 4% PFA and immunostaining for fate markers.

Infection of *in vitro* radial glia cells

Radial Glia cells were plated onto 6-well glass bottom plates (IBLP06-1.5H-N), coated with the above-mentioned substrate. Radial Glia cells were transduced with lentiviral and retroviral particles for 2 hours at 37°C, 5% C02. After washing with non-supplemented

Please cite this article in press as: Wimmer et al., Two translocation mechanisms drive neural stem cell dissemination into the human fetal cortex, Neuron (2026), https://doi.org/10.1016/j.neuron.2026.02.002

media, 2mL of supplemented media was added per well. After 24 to 48 hours of expression of the different constructs, the cells were imaged on a TI2-E inverted video-microscope equipped with a photometric Kinetix sCMOS camera, and each position was imaged every 5 minutes in GFP or RFP with a 10X Plan Fluor, NA: 0.20, WD 15.20 dry objective, using a perfect focus (PFS) mode. To reduce phototoxicity, the laser power was used at the lowest power possible, and the images were binned to increase the fluorescent signal.

Immunostaining of *in vitro* RG cultures

Neural stem cells (NSCs) were cultured on glass coverslips, fixed with 1 mL/well of 4% paraformaldehyde (PFA) for 16 min at room temperature, and washed three times with 1× PBS (10 min each). Coverslips were stored in PBS until use.The blocking/permeabilization solution consisted of 0.1% bovine serum albumin (BSA), 2% donkey serum (1 mL in 50 mL), and 0.1% Triton X-100 (50 μL in 50 mL), prepared in 1× PBS. After aspirating PBS, 1 mL of blocking solution was added per well and incubated for 15–30 min at room temperature. Primary antibodies were diluted in blocking solution and applied as 50–70 μL drops on Parafilm; coverslips were inverted (cell side down) onto the drops and incubated for 2 h at room temperature. Coverslips were returned to wells and washed three times with PBS containing 0.05% Tween-20 (PBST). Secondary antibodies, diluted in blocking solution (with DAPI added when required), were applied using the same procedure and incubated for 2 h at room temperature. After three PBST washes, coverslips were gently dried with lint-free tissue and mounted onto glass slides using aqua-Poly/Mount.

Drug treatments

To inhibit actomyosin contractility, to depolymerize microtubules and inhibit CDK1 activity, *in-vitro* radial glia cells were plated in 6 well plates and brought to a TI2-E inverted video-microscope with a photometric Kinetix sCMOS camera. Each position was imaged every 5 minutes in phase contrast with a 10X Plan Fluor, NA: 0.20, WD 15.20 dry objective, using a perfect focus (PFS) mode. At the start of the movie culture media was supplemented with10μM of blebbistatin; 1μM of nocodazole, 9μM RO-3306, or with a corresponding volume of DMSO.

Culture of glioblastoma cell lines

Patient-derived glioblastoma cells were acquired from the Human Glioblastoma Cell Culture resource (www.hgcc.se) at the Dept. of Immunology, Genetics and Pathology, Uppsala University, Uppsala, Sweden and are a part of collaboration through a Material Transfer Agreement between Institute Curie and Uppsala University.[63] U3008, U3009, U3017, U3021, U3031, U3039, U3047, U3065, U3088, U3123 cell lines from the HGCC biobank were cultured in cell culture plastic dishes coated with Matrigel in culture medium containing 50% DMEM-F12 and 50% Neurobasal Medium, penicillin/streptomycin 1U/mL, B27 (-vitamin A), EGF 10ng/ml and FGF 10ng/ml. At confluency for imaging or for maintenance, cells were detached using pre-warmed accutase and replated in Matrigel coated dishes. Treatment of these cells with nocodazole (1μM), blebbistatin (10μM) or infection with different viral particles and subsequent imaging was done as described for in vitro radial glial cells.

Expression constructs and antibodies

The following plasmids were used in this study: MSCV-IRES-GFP (a gift from Tannishtha Reya (Addgene plasmid # 20672; http://n2t.net/addgene:20672; RRID:Addgene_20672)) pBOB-EF1-FastFUCCI-Puro[45] (a gift from Kevin Brindle & Duncan Jodrell (Addgene plasmid # 86849; http://n2t.net/addgene:86849; RRID:Addgene_86849)); pLV[Exp]-CMV>mCherry(ns):3xGGGGS (VectorBuilder retrievable by the reference VB250528-1313huf); pCAG-VSVG (a gift from Arthur Nienhuis & Patrick Salmon (Addgene plasmid # 35616; http://n2t.net/addgene:35616; RRID:Addgene_35616)), Human EZR shRNA (TF308420, Origene), Human DYNC1H1 shRNA (TL313335, Origene), Human RDX shRNA (TL309884, Origene), Human MSN shRNA (TL311375, Origene), MSCV-IRES-GFP was a gift from Tannishtha Reya (Addgene plasmid # 20672; http://n2t.net/addgene:20672; RRID:Addgene_20672), Human VIM shRNA (TL308419, Origene), Human PAFAH1B1 (LIS1) shRNA (TL310628, Origene), Dominant Negative KASH,

Antibodies used in this study were mouse anti-SOX2 (Abcam Ab79351, 1/500), sheep anti-EOMES (R&D Sytems AF6166, 1/500), rabbit anti-NEUN (Abcam Ab177487, 1/500), chicken anti-GFP (Abcam Ab13970, 1/500), mouse anti-pVimentin (Abcam Ab22651, 1/1000), rabbit anti-NeuroD2 (Abcam, ab104430, 1/500), rabbit anti-HOPX (ProteinTech, 11419-1-AP, 1/500), rabbit anti-NESPRIN2 (Abcam ab204308, 1/500), rabbit anti-PH3 (Abcam ab47297, 1/2000), mouse anti-gamma tubulin (Sigma-Aldrich T5326, 1/1000), rabbit anti-pERM (Cell Signalling Technology, 3141S), mouse anti-LIFR (Abcam 89792, 1/500), rabbit anti-PTPRZ1 (Sigma HPA015103 Atlas antibodies, 1/500), Rabbit anti-pMLC2 (Cell Signalling Technology #3671, 1/1000).

Secondary antibodies used were: Donkey Anti-Sheep IgG H&L (Alexa Fluor 405) Abcam ab175676; DyLight 405 AffiniPure Donkey anti-mouse IgG (H+L) Jackson ImmunoResearch 715-475-150; DyLight 405 AffiniPure Donkey anti-rabbit IgG (H+L) Jackson ImmunoResearch 711-475-152; Alexa Fluor 488 AffiniPure Donkey anti-rabbit IgG (H+L) Jackson ImmunoResearch 711-545-152; Donkey anti-rabbit IgG (H+L) Highly Cross-Adsorbed Secondary antibody, Alexa Fluor Plus 488 Thermo Fisher A32790; Donkey anti-Chicken IgY (H+L) Highly Cross-Adsorbed Secondary antibody, Alexa Fluor 488 Thermo Fisher A78948; Alexa Fluor 488 AffiniPure Donkey Anti-Chicken IgY (IgG) (H+L) Jackson ImmunoResearch 703-545-155; Alexa Fluor 488 AffiniPure Donkey anti-mouse IgG (H+L) Jackson ImmunoResearch 715-545-150; Donkey anti-mouse IgG (H+L) Highly Cross-Adsorbed Secondary antibody, Alexa Fluor Plus 488 Thermo Fisher A32766; Donkey anti-Sheep IgG (H+L) Cross-Adsorbed Secondary antibody, Alexa Fluor 568 Thermo Fisher A21099; Cy3 AffiniPure Donkey Anti-Sheep IgG (H+L) Jackson ImmunoResearch 713-165-147; Donkey anti-mouse IgG (H+L) Highly Cross-Adsorbed Secondary antibody, Alexa Fluor 568 Thermo Fisher A10037; Cy3 AffiniPure Donkey

anti-mouse IgG (H+L) Jackson ImmunoResearch 715-165-150; Donkey anti-rabbit IgG (H+L) Highly Cross-Adsorbed Secondary antibody, Alexa Fluor 568 Thermo Fisher A10042; Cy3 AffiniPure Donkey anti-rabbit IgG (H+L) Jackson ImmunoResearch 711-165-152; Donkey anti-rabbit IgG (H+L) Highly Cross-Adsorbed Secondary antibody, Alexa Fluor Plus 647 Thermo Fisher A32795; Alexa Fluor 647 AffiniPure Donkey anti-rabbit IgG (H+L) Jackson ImmunoResearch 715-605-152; Donkey anti-Goat IgG (H+L) Highly Cross-Adsorbed Secondary antibody, Alexa Fluor Plus 647 Thermo Fisher A32849; Alexa Fluor 647 AffiniPure Donkey Anti-Goat IgG (H+L) Jackson ImmunoResearch 705-605-003; Alexa Fluor 647 AffiniPure Donkey anti-mouse IgG (H+L) Jackson ImmunoResearch 715-605-150.

Bulk RNA-seq library preparation and sequencing

RNA-seq libraries were prepared from 500 ng of total RNA using the *Illumina Stranded Total RNA Prep, Ligation with Ribo-Zero Plus* kit, which performs strand-specific sequencing. The protocol includes enzymatic depletion of abundant transcripts from multiple species (human cytoplasmic and mitochondrial rRNA, mouse and rat rRNA, Gram-positive and Gram-negative bacterial rRNA, and human β-globin transcripts) using probe-based capture. cDNA synthesis was followed by dA-tailing, adaptor ligation with RNA Index Anchors, and PCR amplification with indexed primers (IDT for Illumina RNA UD Indexes; 13 cycles).

Library quality and concentration were assessed using the Qubit dsDNA High Sensitivity Assay (Invitrogen) and the LabChip GX Touch High Sensitivity DNA assay (Perkin – Elmer). Equimolar pooling was performed after quantification by qPCR (KAPA Library Quantification Kit, Roche). Sequencing was carried out on an Illumina NovaSeq X instrument (paired-end 2 × 100 bp), generating ~100 million clusters (≈200 million raw paired-end reads) per sample.

Single-cell reference

We used the developing human neocortex scRNA-seq atlas of[71]as reference, obtained from the UCSC Cell Browser[72]Author-provided cell identities were retained; UMAP and PCA embeddings were used for visualization only.

Pseudobulk construction and bulk RNA-seq

Raw single-cell counts were aggregated by cell type to generate pseudobulk profiles. Bulk RNA-seq counts from GBM tumors were processed in parallel. Gene identifiers (symbols vs. Ensembl) were harmonized using *org.Hs.eg.db*, and duplicate mappings were collapsed by pooling counts across genes mapping to the same identifier.

Normalization and bulk–single-cell similarity

Pseudobulk and bulk matrices were independently normalized with *edgeR* (TMM scaling, log-CPM transformation), and analyses were restricted to intersecting genes. Similarity between pseudobulk cell types and bulk samples was quantified by Spearman correlation.

IST/MST frequency and radial glia identity correlation

To test associations with external scores (e.g., IST+MST fractions), correlations between bulk sample scores and radial glia similarity indices were quantified using Spearman and Pearson statistics, with confidence intervals estimated by bootstrap resampling.

Software for RNA-seq analysis

Analyses were conducted in R (v4.5.x) with Bioconductor (v3.21). Core packages: *Seurat*, *Matrix*, *edgeR*, *limma*, *AnnotationDbi*, *org.Hs.eg.db*, *pheatmap*, *ComplexHeatmap*, *ggplot2*, *ggrepel*, and *reshape2*. All steps were scripted; code is available upon request.

QUANTIFICATION AND STATISTICAL ANALYSIS

Quantitative data are described as mean ± S.D. for $N \geq 3$, except for some human fetal tissue data which are described as $N = 2$, without s.d. No data were excluded from the analyses and the experiments were not randomized. No statistical method was used to predetermine sample size. The investigators were not blinded to allocation during experiments and outcome assessment. Statistical analysis was performed using a two-tailed unpaired Student's t-test using GraphPad Prism 10 software (GraphPad Software). Data distribution was assumed to be normal. *P* values lower than 0.05 were considered statistically significant. The figures were created using Affinity Designer 1.10.